



HAL
open science

Ca and Sr isotope constraints on chemical weathering processes: A view through the Ebro river basin, Spain

Philippe Négrel, Emmanuelle Petelet-Giraud, Catherine Guerrot, Romain Millot

► To cite this version:

Philippe Négrel, Emmanuelle Petelet-Giraud, Catherine Guerrot, Romain Millot. Ca and Sr isotope constraints on chemical weathering processes: A view through the Ebro river basin, Spain. *Chemical Geology*, 2021, 578, pp.120324. 10.1016/j.chemgeo.2021.120324 . hal-03745849

HAL Id: hal-03745849

<https://brgm.hal.science/hal-03745849>

Submitted on 13 Jun 2023

HAL is a multi-disciplinary open access archive for the deposit and dissemination of scientific research documents, whether they are published or not. The documents may come from teaching and research institutions in France or abroad, or from public or private research centers.

L'archive ouverte pluridisciplinaire **HAL**, est destinée au dépôt et à la diffusion de documents scientifiques de niveau recherche, publiés ou non, émanant des établissements d'enseignement et de recherche français ou étrangers, des laboratoires publics ou privés.



Distributed under a Creative Commons Attribution - NonCommercial 4.0 International License

Ca AND Sr ISOTOPE CONSTRAINTS ON CHEMICAL WEATHERING PROCESSES: A VIEW THROUGH THE EBRO RIVER BASIN, SPAIN

Philippe NÉGREL^{a, 1}, Emmanuelle PETELET-GIRAUD^a, Catherine GUERROT^a,
Romain MILLOT^a

a - BRGM, F-45060, Orléans, France

Abstract

The Ebro River (928 km long, 85,530 km² drainage basin) in north-eastern Spain flows into the western Mediterranean Sea through several large cities, and agricultural, mining and industrial areas. The river is one of the largest contributors of freshwater to the Mediterranean and ends in the Ebro delta, one of the most important wetlands in Europe. Bedrock of the Ebro River basin mainly consists of carbonate rocks and evaporites of Paleozoic and Mesozoic age. The Ebro river mainstream was sampled monthly for a year (2006) near the outlet at Amposta, and a field campaign in April of the same year sampled the Ebro along its main course as well as its main tributaries. The behaviour of Ca and its isotopes—combined with that of Sr-isotopes—during water/rock interactions was investigated at the basin scale, with the objective of elucidating the processes controlling the isotope signatures of a large river draining mostly sedimentary bedrock. The $\delta^{44}\text{Ca}_{\text{sw}}$ values (normalized to seawater) ranged from -0.87 to -1.09‰ along the Ebro mainstream, decreasing towards the delta as the Ca content increased. At Amposta, the $\delta^{44}\text{Ca}_{\text{sw}}$ ratio ranged between -0.66 and -1.04‰, with a tendency to decrease with increasing discharge. These variations were similar to those given by the $^{87}\text{Sr}/^{86}\text{Sr}$ values and Sr contents. For the main tributaries, the $\delta^{44}\text{Ca}_{\text{sw}}$ ratio in river waters ranged between -0.43 and -1.04‰, whereas anhydrite-gypsum bedrock values ranged from -0.94 to -1.22‰ and carbonate bedrock from -1.04 to -1.39‰. Comparing Sr-isotope values and Ca/Na ratios showed the role of anhydrite/halide bedrock weathering for some tributaries (Guadalupe, Matarrana, Aragon, Ega), that of carbonate/halide bedrock weathering dominating the others (Gallego, Cinca, Segre), the Ebro mainstream being a mix of both. Bedrock weathering masks the sea-salt signal, if any. As halides contain no Ca, a comparison of $\delta^{44}\text{Ca}_{\text{sw}}$ and $^{87}\text{Sr}/^{86}\text{Sr}$ values further demonstrated the role of anhydrite and limestone for the Ebro and its tributaries, highlighting geochemical processes like carbonate supersaturation in the Guadalupe and Matarrana tributaries.

Keywords: Ebro River, Surface water, Ca isotopes, Sr isotopes, Dissolved load

¹ Corresponding author at: 3 Avenue Claude Guillemin, BP36009 - 45060, Orléans cedex 2, France.
E-mail address: p.negrel@brgm.fr (Ph. Négrel).

35 **1 – Introduction**

36 Calcium is the fifth most abundant element in the Earth's upper continental crust, with an
37 estimated elemental abundance of 25,643 mg/kg (Rudnick and Gao, 2003); it is an essential
38 nutrient for biogeochemical cycles and one of the most concentrated cations in continental
39 surface- and groundwaters. Ca-cycling studies are of primary importance as calcium
40 carbonate precipitation in the ocean is a key process for the carbon balance in the earth/ocean
41 system (Schmitt et al., 2003a; Tipper et al., 2006; 2010). Tracing Ca in the earth system
42 (oceanic cycle, weathering, hydrothermal activity) can be helped by indirect proxies like
43 strontium isotopes, as Sr behaves similarly to Ca (Novak et al., 2020). Over the past decades,
44 the use of Ca isotopes as a direct proxy for calcium behaviour has been developed as well
45 (Zhu and Macdougall, 1998; DePaolo, 2004; Kreissig and Elliott, 2005; Fantle, 2010; 2014;
46 Tipper et al., 2016; Griffith et al., 2020; Griffith and Fantle, 2020). Calcium has six stable
47 isotopes: $^{40}\text{Ca}=96.941\%$, $^{42}\text{Ca}=0.647\%$, $^{43}\text{Ca}=0.135\%$, $^{44}\text{Ca}=2.086\%$, $^{46}\text{Ca}=0.004\%$ and
48 $^{48}\text{Ca}=0.187\%$ (Coplen et al., 2002). Ca isotopes, usually referred to as 44/40 or 44/42 values
49 measured by mass spectrometry (Heuser et al., 2002; Fantle and Bullen, 2009) or MC-ICP-
50 MS (He et al., 2019; Halicz et al., 1999), have the advantage of being direct tracers of Ca-ion
51 sources in the system studied (Fantle, 2010), but—contrary to Sr isotopes—the bulk isotopic
52 fractionation during processes must be considered as well (DePaolo, 2004; Fantle, 2015).

53 In the study of terrestrial systems, Ca isotopes have been used for investigating marine
54 variations (Blättler and Higgins, 2014; Schmitt et al., 2003b; Hensley, 2006), for estimating
55 the Ca-isotope fractionation in bio mineralization (Chang et al., 2004; Gussone et al., 2005;
56 Bradbury et al., 2020), for tracing continental weathering as recorded in the marine cycle over
57 geological time (Fantle and DePaolo, 2005; Blättler et al., 2011; Brazier et al., 2015; Du
58 Vivier et al., 2015), or for investigating the marine calcium cycle (Zhu and Macdougall,
59 1998). Ca isotopes were also used to identify hydrothermal pathways (Amini et al., 2008;

60 Scheuermann et al., 2018) and, recently, to investigate the composition of oceanic crust (Chen
61 et al., 2020a) or subduction processes (Lu et al., 2020). Tracking continental weathering was
62 investigated in aquifers (Jacobson and Holmden, 2008; Jacobson et al., 2015; Li et al., 2018)
63 and in catchments (Schmitt et al., 2005; Tipper et al., 2006; Ryu et al., 2011; Hindshaw et al.,
64 2011; 2013; Moore et al., 2013; Chen et al., 2020b). Finally, in order to assess the factors
65 involved in long-term Ca cycling in terrestrial environments, Ca-isotope studies were applied
66 to soils and plants in ecosystems (Wiegand et al., 2005; Cenki-Tok et al., 2009; Holmden and
67 Bélanger, 2010; Schmitt et al., 2012; Brazier et al., 2019).

68 Additionally, strontium isotopes have been used extensively in the earth sciences as
69 tracers of seawater evolution through time (Veizer, 1989), in environmental investigations
70 (Åberg, 1995) to study weathering and sediment transport by rivers (Goldstein and Jacobsen,
71 1987; Palmer and Edmond, 1992; Petelet-Giraud et al., 2003), whether as dissolved or
72 suspended loads (Négrelet and Grosbois, 1999; Négrelet et al., 2000; English et al., 2000; Wei et
73 al., 2013), and ranging from diluted rain water (Chabaux et al., 2005) to highly saline mineral
74 waters (Négrelet et al., 1997; Millot et al., 2007).

75 Past investigations of the Ebro River catchment studied long-term fluxes of dissolved
76 and suspended matter (Négrelet et al., 2007), dissolved fluxes recording the impact of main
77 lithologies and the role of tributaries (Petelet-Giraud and Négrelet, 2011), as well as hydrogen
78 and oxygen isotopes (Négrelet et al., 2016). In this paper, we focus on Ca- and Sr-isotope data
79 from the dissolved load of 25 river-water samples collected in the Ebro River basin. We
80 measured calcium and strontium and their isotope values in all reservoirs and parts of the
81 basin affected by various processes, such as weathering, mixing of water and anthropogenic
82 input. All of these processes must be investigated as the Mediterranean areas of both southern
83 Europe and North Africa are subject to dramatic changes that will affect the sustainability,
84 quantity, quality, and management of water resources (García-Ruiz et al., 2011) and, more

85 precisely, the Ebro River and its tributaries in north-eastern Spain that are regulated by over
86 187 dams (Batalla et al., 2004) impacting the water cycle (Négrel et al., 2016).

87 We first define the Ca cycling in a river basin affected by—mainly climatic—impacts
88 (drought and water deficit) and regarding water use (agriculture, water reservoirs and
89 industry), all in the context of global climate change.

90 Secondly, we study the important mechanism known to fractionate Ca isotopes, i.e. the
91 incorporation of light Ca isotopes during precipitation from a solution (DePaolo, 2004;
92 Gussone et al., 2005; Fantle, 2015) and its consequences on the Ca cycle. For this, we
93 investigated the source rocks of Ca, for Ca and Sr isotopes at the river basin scale. Then we
94 compared the mass-dependent fractionation of Ca isotopes during rock weathering to the Sr
95 isotopes that are direct tracers of the source rock.

96 Finally, we discuss the fractionation of Ca isotopes by precipitation of dissolved Ca as
97 solid phases, focusing on this process compared to the Sr isotopes that are not affected by
98 precipitation.

99 **2 - General setting**

100 The Ebro river (Fig. 1) in north-eastern Spain rises near the Atlantic coast in the Cantabrian
101 Mountains and flows into the western Mediterranean Sea through several large cities and
102 agricultural, mining and industrial areas. The Ebro is 928 km long, has an 85,530 km²
103 drainage basin, and is the largest Spanish river system, being one of the largest contributors of
104 freshwater to the Mediterranean Sea. The Ebro River basin area hosts 2.8 million inhabitants,
105 the majority (46%) living in the following cities: Irun (Pamplona), Lleida, Logroño, Vitoria,
106 Zaragoza and Huesca (CHE, <http://www.chebro.es/>).

107 The catchment area is heterogeneous in terms of geology, topography and land use,
108 but the most heterogeneous parameter is climate, the basin being divided into four main

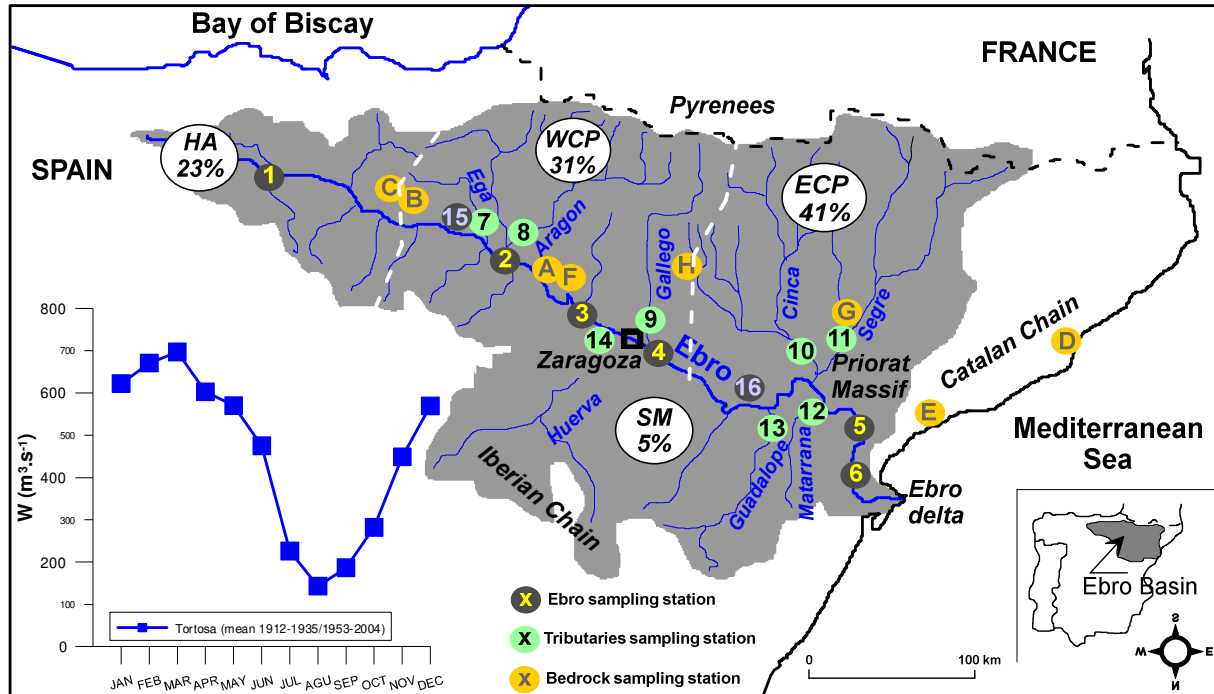
109 climatic areas with different degrees of runoff impoundment. These are the Atlantic
110 headwaters with an average annual precipitation of about 900 mm, the west-central Pyrenees
111 (about 950 mm), the eastern Pyrenees (about 800 mm) and the southern Mediterranean zone
112 (about 500 mm), with a relative runoff contribution to the river for these four climatic zones
113 of 23%, 31%, 41% and 5%, respectively (Batalla et al., 2004).

114 The Ebro basin is underlain by several rock types:

- 115 1) Sedimentary and metamorphic Paleozoic rocks of the Iberian Chain and Pyrenees
116 mountains, the igneous rocks of these two areas, and the Priorat Massif.
- 117 2) Sedimentary Mesozoic rocks of the Iberian Chain, an intraplate mountain range that
118 occupies the north-eastern part of the Iberian Peninsula and forms the southern margin of
119 the Ebro basin. It consists of rocks that cover most of the Phanerozoic stratigraphic
120 record, though Jurassic and Cretaceous carbonate rocks predominate.
- 121 3) Sedimentary Tertiary rocks of the Pre-Pyrenees and the Ebro Valley.
- 122 4) Neogene deposits filling a depression through which the lower part of the Ebro River
123 flows, which then bends through the Catalan Chain and the Baix Ebro Valley before
124 flowing across delta-plain deposits into the sea (Guillén and Palanques, 1992). The
125 occurrence of evaporite deposits in the Ebro River basin has been documented in detail
126 (Castillo Herrador, 1974; Elorza and Santolalla, 1998 and references therein).

127 The Ebro River basin is made up of several tributary streams whose location is shown
128 on Figure 1 and summarized in Table 1. In the northern part of the basin, the main Ebro
129 tributaries from upstream to downstream are the Aragon, Gallego, Cinca and Segre rivers.
130 These drain silicate rocks of the Pyrenees in their upper part, whereas downstream they
131 integrate water flowing over and from the sedimentary rocks of the Ebro basin. The Ega River
132 catchment, a tributary in the upper part of the basin, is composed of sedimentary and
133 metamorphic Palaeozoic and Mesozoic rocks of the Iberian Chain. In the southern part of the

134 basin, the main tributaries are the Huerva, Guadalupe and Matarrana from upstream to
 135 downstream, whose waters only flow over sedimentary rocks and basin deposits.
 136



137
 138 *Figure 1. Location of the Ebro basin in Spain, schematic location of the sampling points in*
 139 *the basin. The main river was sampled upstream and downstream from the confluences of the*
 140 *main tributaries, numbers 1 to 5; the tributaries were sampled (numbers 7 to 14). In addition,*
 141 *the Ebro outlet at Amposta (N° 6; Cruzado et al., 2002) was sampled each month between*
 142 *June 2005 and May 2006. Groundwater was also sampled at two locations in the Ebro basin*
 143 *(N° 15 Andosilla in Navarra; irrigation well at 6 m depth and N° 16 Lleida; irrigation well at*
 144 *7 m depth). A to H, representative bedrock sample locations. The four main climatic areas of*
 145 *the Ebro Basin as defined by Batalla et al. (2004) are indicated with the percentages of the*
 146 *total runoff: Humid Atlantic (HA) covering the headwaters (average annual precipitation 900*
 147 *mm), Western Central Pyrenees (WCP; 950 mm), Eastern Central Pyrenees (ECP; 800 mm),*
 148 *and Southern Mediterranean (SM; 500 mm).*
 149

150 In the Ebro basin, agricultural land covers nearly 60% of the surface area, combined
 151 with grassland, savannah and shrub. Urban and industrial areas account for 14% of land use,
 152 forest covers 5% of land and wetlands make up the remaining 1% of land area in the basin.
 153 Most urban and industrial zones are located in the valleys, around the major rivers, the Ebro
 154 in particular. Industrial activities mostly involve construction, secondary metals, textile, food
 155 and hydroelectricity.

156 The total mean annual runoff is approximately $6,837.10^6 \text{ m}^3$, the total water storage
157 capacity of the 187 reservoirs that regulate water flow in the basin being around 57%. The
158 northern tributaries contribute more to the discharge than those in the south, as the drainage
159 basins of the former are located in higher rainfall areas (Batalla et al., 2004). Mendavia station
160 is located on the Ebro about 10 km upstream of 1, Lodosa station; Table 1, Fig. 1). Upstream
161 from Mendavia, three dams exist on the Ebro River and eight on its tributaries, while between
162 Mendavia and Tortosa, the number of active dams is respectively 4 and 41 (Confederación
163 Hidrográfica del Ebro [CHE], <http://www.chebro.es/>). Monthly water discharge of the Ebro
164 significantly decreased over the last century (op. cit.), which is mainly attributed to increased
165 water use—with its attendant evaporation—for human activities (irrigation, reservoirs,
166 electricity production and domestic consumption). Its natural flow at the outlet of the basin
167 was around $590 \text{ m}^3 \cdot \text{s}^{-1}$ between 1914 and 1935, but between 1960 and 1990 it had reduced by
168 28% to $430 \text{ m}^3 \cdot \text{s}^{-1}$ (Ibáñez et al., 1996). Irrigation is the main water user in the basin with
169 almost 700,000 irrigated hectares and a total water demand of $6310 \cdot 10^6 \text{ m}^3 \cdot \text{y}^{-1}$ (op. cit.).
170 Surface waters irrigate 91% of the land, and groundwater irrigates the rest (INE, 2003).
171 Irrigation causes a major hydraulic deficit, with an average of around $300 \text{ m}^3 \cdot \text{s}^{-1}$ abstracted
172 from the rivers. Furthermore, large hydroelectric power plants in the Ebro system supply 50%
173 of Spain's electricity. According to recent work on potential alteration in the Ebro basin by
174 García and Moreno (2000), only the Ebro headwater tributaries still have natural flow, the
175 fluvial regimes of the main tributaries reaching the Ebro in the central and lower parts of the
176 catchment (Segre, Cinca, Gallego and Aragon rivers) being slightly to moderately altered.

177 A general mass balance equation for the budget of chemical elements in river water load
178 can be formulated as follows in Eq. 1 (Grosbois et al., 2000, and references therein):

179
$$\text{rock weathering} + \text{atmospheric input} + \text{human activities input} = \text{dissolved load} + \text{solid load} \text{ (Eq. 1)}$$

180

181 The Ebro basin encompasses a gradient from Atlantic to Mediterranean climates, and
182 has a remarkably complex topography, geology and land cover. However, the basin is highly
183 regulated by dams for producing hydropower and supplying water for agriculture. These
184 geographical and land-use characteristics explain why sub-basins of the Ebro River basin
185 present quite different hydrological behaviours (Négrel et al., 2016). Dams on the Ebro Basin
186 play an important role in controlling solid matter fluxes and regulating water flow (Batalla et
187 al., 2004). This explain the low suspended particulate matter concentration over the basin
188 (Négrel et al., 2007) and lack of relationship with the discharge of the river. This minimizes
189 the role of the solid load in the mass balance equation 1.

190 A conceptual scheme of the Ebro hydrosystem on the basis of H₂O isotope signatures,
191 chlorine concentrations and river discharge, shows the origin of water masses at the basin
192 outlet according to the different hydrological periods (Négrel et al., 2016). It also highlights
193 the major role of the numerous dams that regulate the flow of the Ebro and its tributaries
194 throughout the year, modifying the natural functioning of the catchment as also shown by the
195 dissolved solute concentrations for instance.

196 As a whole, the conceptual seasonal scheme of the Ebro hydrosystem showed that,
197 during springtime, the Ebro water at its outlet comes straight from the climatic areas (i.e. the
198 main tributaries), with few damming effects on the discharge. During autumn, most river
199 water is supplied by the central part of the basin, groundwater supplying most of the river
200 flow. At the same time, water retention in the different climatic areas by dam impoundment is
201 likely as river discharge is low. During summer, discharge is sustained by the reservoirs and
202 the water origin is clearly from the climatic areas, the river discharge remaining low like that
203 observed during autumn. Finally, during winter, river-water supply starts with a remanent
204 groundwater influence, after which the climatic areas become predominant. However,
205 wintertime is not the main period of groundwater supply to the river system and we may again

206 suspect that water in the different climatic areas is retained in reservoirs, as during autumn.
207 Thus, a time-related term should exist in the mass-balance equation for the chemical budget
208 of the Ebro river.

209 **3 – Samples, material and methods**

210 ***3.1. Sampling of water and rocks***

211 The Ebro River and its main tributaries were sampled during a field campaign in April 2006.
212 The sampled tributaries correspond to the main water input to the Ebro, draining the main
213 rock types in the basin (Fig. 1). The Ebro was sampled upstream and downstream from the
214 confluences of these main tributaries (Fig. 1, 1 to 5). In addition, the Ebro outlet at Amposta
215 (6, Fig. 1; Cruzado et al., 2002) was sampled each month between June 2005 and May 2006,
216 in order to monitor temporal compositional variations in river flow. Water samples were
217 collected in the middle of each stream channel from bridges. Flow records for 171 gauging
218 stations in the Ebro basin are available from the Confederación Hidrográfica del Ebro
219 (<http://www.chebro.es/>). Groundwater was also sampled at two locations in the Ebro basin
220 (Fig. 1: E15 Andosilla, irrigation well at 6 m depth; E16 Lleida, irrigation well at 7 m depth),
221 to provide a broad idea of the geochemical signature of potential groundwater input to surface
222 water.

223 Representative bedrock samples were collected along the Ebro (Fig. 1, A to H). Three
224 lithologies were considered in the sampling strategy: gypsum-anhydrite (4 samples) and
225 carbonate rock (4 samples). Gypsum samples were collected in Navarra: the Ablitas sample
226 (Fig 1, A) represents Miocene continental deposits and the Mafieru sample (Fig. 1, B) is from
227 Oligocene continental deposits. One anhydrite sample was collected in the Navarra Potash
228 Basin (Fig. 1, C) from an Eocene marine deposit, and the second one, collected in Espinagosa
229 near Barcelona (Fig. 1, D) is from from Triassic (Keuper) deposits.

230 Carbonate rock (limestone) was collected in several places. Triassic Muschelkalk was
 231 sampled from a core (5.50 m depth) at Baix near Tarragona (Fig. 1, E). A continental
 232 Miocene limestone was collected in the same place as the Ablitas gypsum sample (Navarra,
 233 Fig. 1, F); a continental Paleocene (Garumnian) carbonate facies was sampled at Tremp (near
 234 Lleida, Fig. 1, G). Finally, Oligocene limestone was collected in Fraga near Huesca, Fig. 1, H.

235 *Table 2: Samples reference, type, sampling stations and their locations.*

Reference	Type	Name	Location
1	Main river	Ebro	Miranda
2	Main river	Ebro	Lodosa
3	Main river	Ebro	Gallur
4	Main river	Ebro	Presa de Pina
5	Main river	Ebro	Tortosa
6	Outlet	Ebro	Amposta
7	Tributary	Ega	Andosilla
8	Tributary	Rio Aragon	Milagro
9	Tributary	Rio Galliégo	Before confluence
10	Tributary	Rio Huerva	Zaragosa
11	Tributary	Rio Guadalope	Before confluence
12	Tributary	Rio Matarrana	Nonaspe
13	Tributary	Rio Cinca	Fraga
14	Tributary	Rio Segre	Before confluence
15	Groundwater	E15	Andosilla
16	Groundwater	E16	LLeida
A	Rock	Gypsum	Ablitas
B	Rock	Gypsum	Mafieru
C	Rock	anhydrite	Navarra
D	Rock	anhydrite	Espinagosa
E	Rock	Carbonate	Baix
F	Rock	Carbonate	Ablitas
G	Rock	Carbonate	Tremp
H	Rock	Carbonate	Fraga

236

237 **3.2 Methods**

238 After collection, the water samples were filtered through pre-cleaned 0.45 µm acetate filters;
 239 100 mL were acidified with double-distilled nitric acid to pH<2 and stored in pre-cleaned
 240 polyethylene bottles for major-cation analyses, and a further 100 mL were stored unacidified

241 in polyethylene bottles for anion analysis. The water samples were analysed by ion
242 chromatography for major anions and by inductively coupled plasma-atomic emission
243 spectrometry (ICP-AES) for Ca, Na, K and Mg, by ICP-MS for trace elements (accuracy 5-
244 10%), and by Gran's method (HCl titration) for alkalinity.

245 Chemical purification of around 3 μg Sr was done in an ion exchange column (Sr-
246 Spec) before mass analysis, according to a method adapted from Pin and Bassin (1992), with
247 total blank <1 ng for the entire chemical procedure. After chemical separation, around 150 ng
248 of Sr was loaded onto a W filament with Ta activator and analysed for Sr isotopes in static
249 mode with a Finnigan MAT 262 multi-collector thermal ionization mass spectrometer
250 (TIMS). The $^{87}\text{Sr}/^{86}\text{Sr}$ values were normalized to a $^{86}\text{Sr}/^{88}\text{Sr}$ ratio of 0.1194. An average
251 internal precision of $\pm 10 \times 10^{-6}$ ($2\sigma_m$) was obtained during this study. The reproducibility of
252 the $^{87}\text{Sr}/^{86}\text{Sr}$ ratio measurements was tested by repeated analyses of the NBS987 standard, for
253 which a mean value of $0.710243 \pm 18 \times 10^{-6}$ (2σ , $n=93$) was obtained during the overall
254 period of analysis (09/2005-10/2008). Sample ratios were normalized to the certified value of
255 the NBS987 (0.710240) as compared to the measured value.

256 Ca isotopic ratios were measured with a Finnigan MAT 262 multi-collector mass
257 spectrometer, using a ^{42}Ca - ^{48}Ca double-spike for instrumental mass discrimination correction.
258 To minimize error propagation, the amount of double spike added will lead in the mixture to
259 more than 95% of ^{42}Ca and ^{48}Ca derived from the double spike and more than 95% of ^{40}Ca
260 and ^{44}Ca derived from the sample. After equilibration and evaporation of a sample-spike
261 mixture, purification of around 5 to 6 μg of calcium from the matrix was done on AG50W-X8
262 cationic resin. Procedural blank were between 25 to 40 ng and thus negligible. Around 1 μg of
263 purified Ca was loaded onto Ta single filaments.

264 The data were obtained in dynamic multiple-collection mode in two steps.
265 1) Simultaneous analysis of ^{40}Ca , ^{41}K masses (to check the absence of isobaric interference of

266 ^{40}K on ^{40}Ca), ^{42}Ca and ^{43}Ca ; 2) Simultaneous analysis of ^{44}Ca and ^{48}Ca masses. Samples are
267 always run twice, the internal precision ($2\sigma_m$) of individual analyses is better than 0.10‰. The
268 reproducibility of sample measurements (2σ) ranged between ± 0.04 and 0.15‰. The
269 reproducibility (2σ) obtained by repeated analyses of seawater and NIST 915a was $\pm 0.20\%$.
270 The mean value obtained on NIST 915a was $-1.89 \pm 0.20\%$ (2σ , $n=35$) and consistent with
271 published data. The $^{44/40}\text{Ca}$ isotope values are shown as $\delta^{44}\text{Ca}$ values and are reported
272 compared to seawater (sw).

273 Bedrock samples were dissolved in ultrapure water for evaporite samples and with
274 sub-boiled HCl for carbonates. After dissolution, major- and trace elements, and Sr- and Ca
275 isotopes were determined following the same procedure as for water.

276 To obtain mineral-saturation indices for river-water samples, major-ion concentrations
277 and field parameters (T, pH, and alkalinity) were input into PHREEQC software with an
278 improved lln.dat thermodynamic database (Parkhurst and Appelo, 1999). This calculated ion
279 activity, activity coefficients, and saturation indexes SI for calcite, aragonite and dolomite.

280 **4 – Results**

281 Table 2 contains data for the different bedrocks and Table 3 contains all analytical results for
282 river water and groundwater.

283 **4.1. The bedrock**

284 The highest Ca contents are found in continental Paleocene and Oligocene carbonate facies G
285 and H (maximum around 420 mg.g^{-1}) and a low Sr content (around $500 \mu\text{g.g}^{-1}$), for a Ca/Sr
286 molar ratio of around 1460-1500. The lowest Ca value is for Triassic Muschelkalk, sample E,
287 with a Ca content around 230 mg.g^{-1} and a Sr content of around $120 \mu\text{g.g}^{-1}$, and a Ca/Sr molar
288 ratio of 3000. The highest Sr contents are for anhydrite, ranging from $2380 \mu\text{g.g}^{-1}$ in Triassic

289 anhydrite (sample D), up to 4590 $\mu\text{g}\cdot\text{g}^{-1}$ in the sample collected in the Potash Basin in Navarra
 290 (sample C). This gives Ca/Sr molar ratios of 130 and 270, respectively.

291 $^{87}\text{Sr}/^{86}\text{Sr}$ versus Sr content varies with the type of bedrock; $^{87}\text{Sr}/^{86}\text{Sr}$ ratio data are
 292 scattered for carbonate bedrock, with values ranging from 0.70779 to 0.70918 and Sr contents
 293 varying from 120 up to 1035 $\mu\text{g}\cdot\text{g}^{-1}$. Evaporite bedrock, however, displays $^{87}\text{Sr}/^{86}\text{Sr}$ ratios
 294 from 0.70766 to 0.70830 and Sr contents varying between 2380 and 4590 $\mu\text{g}\cdot\text{g}^{-1}$.

295

296 *Table 2: Rock type (gypsum, anhydrite and carbonate), sample ID, $\delta^{44}\text{Ca}_{\text{sw}}$, Ca, Na and SO_4*
 297 *content, $^{87}\text{Sr}/^{86}\text{Sr}$ ratio and Sr content for the different bedrocks.*
 298

Type	Samples	Station	$\delta^{44}\text{Ca}_{\text{sw}}$	2σ	Ca mg g^{-1}	Na mg g^{-1}	SO_4 mg g^{-1}	$^{87}\text{Sr}/^{86}\text{Sr}$	Sr $\mu\text{g g}^{-1}$
gypsum	ABI-2	A	-1.17	0.03	250	0.1	378	0.70818	2892
gypsum	MN14	B	-1.07	0.09	254	0.6	377	0.70830	2499
anhydrite	S3	C	-1.22	0.01	316	2.7	378	0.70781	4590
anhydrite	TRIAS	D	-0.94	0.10	300	0.4	396	0.70766	2379
carbonate	S3 5.50m	E	-1.39	0.13	231	0.7	-	0.70872	120
carbonate	ABC-4	F	-1.04	0.01	376	1.2	-	0.70822	1035
carbonate	SA-40	G	-1.07	0.11	424	0.4	-	0.70779	511
carbonate	LFr2 14	H	-1.18	0.07	415	0.8	-	0.70918	571
halide	HALITE	Halides	-0.72	0.08	-	-	-	0.70864	2

299

300 *Table 3: Sample ID, distance to Ebro source, river discharge ([CHE]), $\delta^{44}\text{Ca}_{\text{sw}}$, $^{87}\text{Sr}/^{86}\text{Sr}$*
 301 *ratio and Sr content, major ions for surface water (Ebro survey at the Amposta station, Ebro*
 302 *main stream, tributaries, Fig. 1) and groundwater (Fig. 1) in the Ebro River Basin. Cl*
 303 *concentrations are from Négre et al., 2016).*
 304

Samples	Station	Sampling date	Distance to the source km	Discharge $\text{m}^3 \text{s}^{-1}$	$\delta^{44}\text{Ca}_{\text{sw}}$	2σ	$^{87}\text{Sr}/^{86}\text{Sr}$	Sr $\mu\text{g L}^{-1}$	Ca $\mu\text{g L}^{-1}$	Na $\mu\text{g L}^{-1}$	Mg $\mu\text{g L}^{-1}$	K $\mu\text{g L}^{-1}$	Cl $\mu\text{g L}^{-1}$	SO_4 $\mu\text{g L}^{-1}$	NO_3 $\mu\text{g L}^{-1}$	HCO_3 $\mu\text{g L}^{-1}$
Ebro survey Amposta Station																
jun.	E6	6/15/2005	552	150.7	-0.96	0.15	0.70847	1150	109	65	17	3	104	138	11	200
jul.	E6	7/15/2005	552	141.6	-0.87	0.11	0.70848	1370	112	77	19	3	122	166	9	201
Aug.	E6	8/11/2005	552	119.0	-0.77	0.02	0.70854	1759	125	141	28	6	240	182	7	202
Sep.	E6	9/20/2005	552	124.5	-0.66	0.02	0.70859	2437	144	171	36	6	277	260	7	208
Oct.	E6	10/10/2005	552	118.3	-0.77	0.04	0.70854	2488	140	239	43	6	389	308	6	194
Nov.	E6	11/14/2005	552	120.8	-0.80	0.03	0.70857	2660	137	245	44	9	420	315	10	180
Dec.	E6	12/21/2005	552	300.0	-0.93	0.06	0.70844	2490	147	142	32	4	212	308	11	212
Jan.	E6	1/17/2006	552	402.3	-1.04	0.05	0.70841	1940	123	97	24	4	147	223	14	213
Feb.	E6	2/15/2006	552	173.0	-0.73	0.06	0.70850	1540	116	84	21	4	119	185	14	208
Mar.	E6	3/14/2006	552	452.0	-0.81	0.04	0.70842	1180	104	65	16	3	95	139	13	203
Apr.	E6	4/19/2006	552	202.1	-0.72	0.05	0.70849	1250	96	69	18	3	109	152	11	175
May	E6	5/22/2006	552	225.3	-0.86	0.04	0.70858	1120	86	55	15	3	86	131	-	192
Ebro main stream																
Miranda	E1	04/18-20-2006	104	-	-0.87	0.03	0.70864	704	93	48	13	2	54	113	14	229
Lodosa	E2	04/18-20-2006	241	68.2	-0.93	0.06	0.70856	855	88	42	13	2	53	115	12	176
Gallur	E3	04/18-20-2006	281	97.1	-0.93	0.002	0.70837	1440	107	96	20	3	130	162	16	223
Presa de Pina	E4	04/18-20-2006	336	105.9	-1.09	0.04	0.70842	1850	134	138	26	5	208	240	18	250
Tortosa	E5	04/18-20-2006	543	138.0	-1.07	0.002	0.70849	1270	108	70	19	3	111	154	9	205
Tributaries																
Ega	E7	04/18-20-2006	216	7.8	-1.01	0.02	0.70807	1210	139	128	20	6	191	164	17	290
Aragon	E8	04/18-20-2006	233	9.4	-1.04	0.03	0.70814	973	86	88	14	4	131	88	9	253
Galliego	E9	04/18-20-2006	328	2.6	-1.00	0.02	0.70861	1750	137	223	21	4	324	255	4	179
Huerva	E10	04/18-20-2006	324	-	-0.81	0.02	0.70862	3200	220	101	60	8	131	560	19	264
Guadalope	E11	04/18-20-2006	397	80.9	-0.73	0.04	0.70786	5090	276	68	98	7	69	864	9	216
Matarrana	E12	04/18-20-2006	457	3.8	-0.43	0.001	0.70796	1280	70	21	45	4	36	167	17	223
Cinca	E13	04/18-20-2006	422	0.2	-0.78	0.09	0.70877	1550	99	118	25	3	146	197	6	226
Segre	E14	04/18-20-2006	422	3.0	-1.00	0.03	0.70897	1840	109	53	24	3	56	212	11	201
Groundwater																
G15	E15	04/18-20-2006	200	-	-0.84	0.06	0.70840	7400	557	732	236	77	1120	1870	88	370
GA-2	E16	04/18-20-2006	370	-	-0.87	0.06	0.70847	3020	233	262	53	3	408	508	56	337

305

306

307 Further relationships can be seen in the variation of $\delta^{44}\text{Ca}$ versus Ca contents. The

308 $\delta^{44}\text{Ca}_{\text{sw}}$ in carbonate bedrock varies from -1.04 to -1.39‰ and Ca contents are in the range of

309 231 to 424 $\mu\text{g}\cdot\text{g}^{-1}$, while evaporite bedrock has $\delta^{44}\text{Ca}_{\text{sw}}$ values ranging from -0.94 and -1.22‰
310 and a Ca content in the range of 250 to 316 $\mu\text{g}\cdot\text{g}^{-1}$, the $\delta^{44}\text{Ca}_{\text{sw}}$ range of the bedrock being
311 similar to published values (Russell et al., 1978; Skulan et al., 1997; De La Rocha and
312 DePaolo, 2000; Jacobson and Holmden, 2008; Blättler and Higgins, 2014). A cross plot of the
313 $\delta^{44}\text{Ca}_{\text{sw}}$ vs. $^{87}\text{Sr}/^{86}\text{Sr}$ values (not shown) does not show any relationship with R^2 around 0.3.

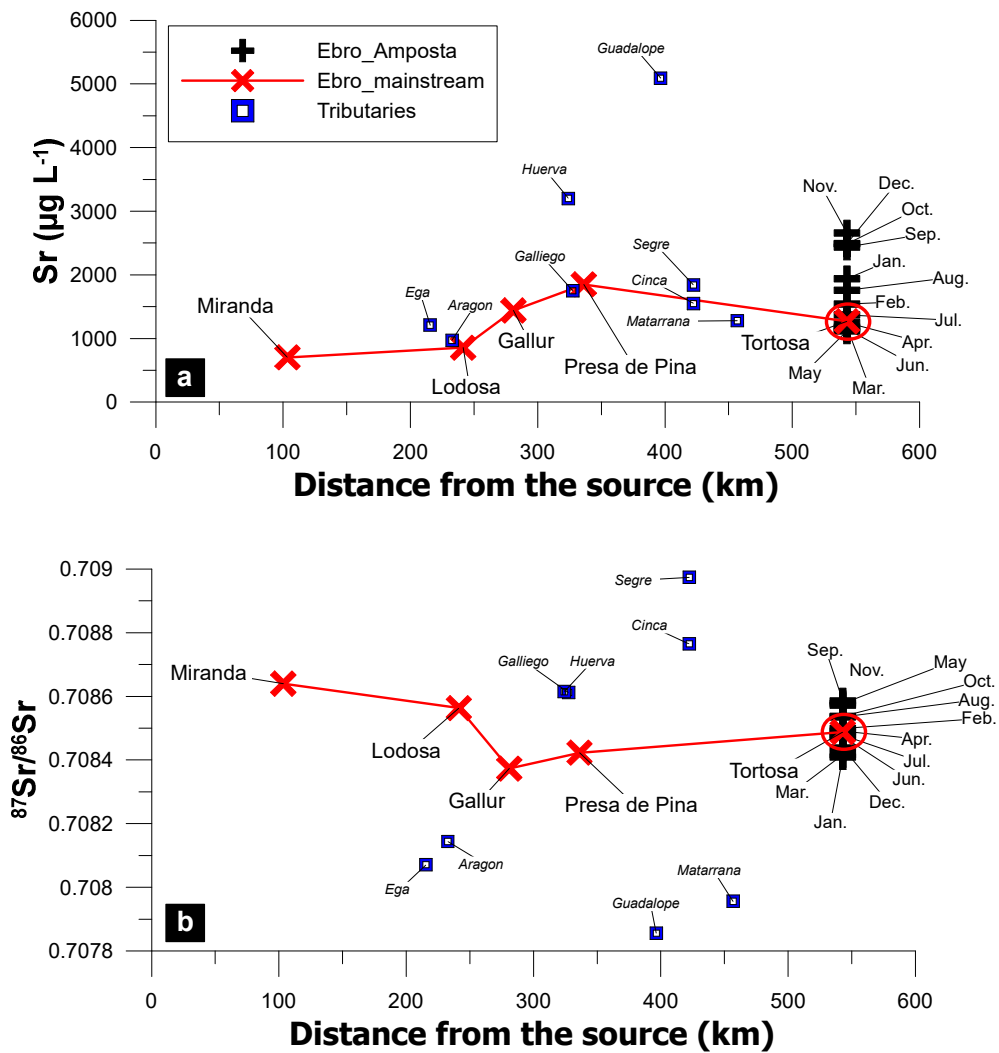
314 Note that the lowest observed $^{87}\text{Sr}/^{86}\text{Sr}$ ratio in Triassic anhydrite (sample D) has the
315 highest $\delta^{44}\text{Ca}_{\text{sw}}$, but the highest $^{87}\text{Sr}/^{86}\text{Sr}$ values (>0.7086) correspond to different $\delta^{44}\text{Ca}_{\text{sw}}$
316 values (-1.18 and -1.39‰).

317 **4.2. Tributaries, the main Ebro stream and the outlet survey**

318 The eight sampled tributaries of the Ebro River (Fig. 1, numbers 7 to 14) showed $^{87}\text{Sr}/^{86}\text{Sr}$
319 ratios ranging from 0.70786 for the Rio Guadalupe (with the highest Sr content at 5090 $\mu\text{g}\cdot\text{L}^{-1}$
320 ¹) up to 0.70897 for the Rio Segre (Sr content around 1840 $\mu\text{g}\cdot\text{L}^{-1}$). The lowest Sr content was
321 970 $\mu\text{g}\cdot\text{L}^{-1}$ for the Rio Aragon with an intermediate $^{87}\text{Sr}/^{86}\text{Sr}$ ratio of 0.70814. For $\delta^{44}\text{Ca}_{\text{sw}}$, the
322 values ranged between -0.43‰ in the Rio Matarrana to -1.04‰ for the Rio Aragon, both
323 rivers having low Ca contents (70 and 86 $\text{mg}\cdot\text{L}^{-1}$, respectively). The highest Ca contents were
324 in the Rio Guadalupe and Rio Huerva (276 and 220 $\text{mg}\cdot\text{L}^{-1}$, respectively) with $\delta^{44}\text{Ca}_{\text{sw}}$ values
325 of around -0.73‰ and -0.81‰.

326 Along the main Ebro stream, the samples were collected from 100 km to 450 km
327 below the river source, just upstream of where a monthly monitoring sample was collected at
328 the same time (Fig. 2a-b). The Sr content in April samples collected along the Ebro increased
329 from 704 $\mu\text{g}\cdot\text{L}^{-1}$ in the farthest upstream point, to 1850 $\mu\text{g}\cdot\text{L}^{-1}$ around 350 km downstream
330 and then decreased to 1270 $\mu\text{g}\cdot\text{L}^{-1}$ in the last point before the outlet-survey location where the
331 Sr content was 1250 $\mu\text{g}\cdot\text{L}^{-1}$. This variation reflects the values found in the tributaries near the
332 mainstream. At Amposta, the Sr contents varied between 1120 $\mu\text{g}\cdot\text{L}^{-1}$ in May and 2660 $\mu\text{g}\cdot\text{L}^{-1}$
333 in November. Up to 250 km downstream, the $^{87}\text{Sr}/^{86}\text{Sr}$ ratio first decreased slightly, from

334 0.70864 in Miranda de Ebro to 0.70837 at Gallur, and then increased to 0.70849 in Tortosa.
 335 Concerning the Sr content, the $^{87}\text{Sr}/^{86}\text{Sr}$ ratio variation along the mainstream fully agreed with
 336 the values found at tributary junctions and their cumulative impact. At Amposta, the $^{87}\text{Sr}/^{86}\text{Sr}$
 337 ratio ranged from 0.70841 in January to 0.70859 in September, but roughly similar values
 338 were observed in May (0.70857) and November (0.70858).



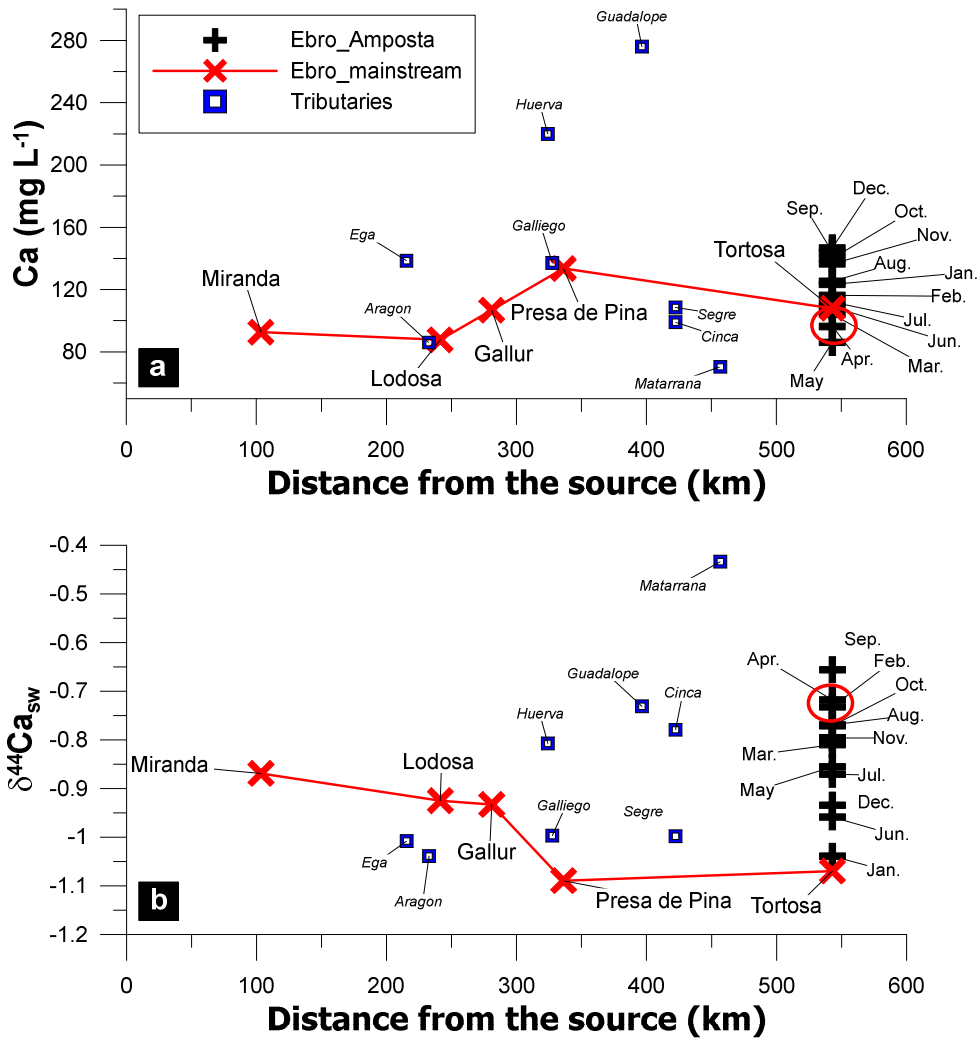
339
 340 *Figure 2a, b. Variation of the Sr concentration ($\mu\text{g.L}^{-1}$) and $^{87}\text{Sr}/^{86}\text{Sr}$ ratio from the Ebro*
 341 *headwaters (0 km) to the outlet (550 km,) for the Ebro mainstream and its tributaries. The*
 342 *variations at the outlet (Amposta) are shown and the sampling month indicated; the red circle*
 343 *marks the sampling at Amposta at the same time as that of the Ebro mainstream.*
 344

345 The two groundwater samples had similar $^{87}\text{Sr}/^{86}\text{Sr}$ ratios (0.70840-0.70847) and $\delta^{44}\text{Ca}_{\text{sw}}$
 346 values (-0.84 - -0.87‰), for sample E15 (Andosilla in Navarra; irrigation well at 6 m depth)
 347 and E16 (LLeida; irrigation well at 7 m depth) respectively, but they differed in their chemical

348 contents. Sample E15 had a higher Sr content ($7400 \mu\text{g.L}^{-1}$) than sample E16 ($3020 \mu\text{g.L}^{-1}$), as
349 well as higher Ca and SO_4 contents (557 mg.L^{-1} and 1870 mg.L^{-1} , respectively) than sample
350 E16 (233 mg.L^{-1} and 508 mg.L^{-1} , respectively).

351 The Ca content in tributaries, mainstream and outlet-survey samples plotted against
352 the distance from the Ebro source mimics that of Sr (Fig. 3a, b). The $\delta^{44}\text{Ca}_{\text{sw}}$ ratio along the
353 mainstream decreased continually from -0.92 at Miranda de Ebro to -1.13‰ at Presa de Pina
354 and Tortosa, a decrease that disagrees with the lowest values observed in the Galliego and
355 Segre tributaries with $\delta^{44}\text{Ca}_{\text{sw}}$ around -1.03‰ . At Amposta, the $\delta^{44}\text{Ca}_{\text{sw}}$ values ranged
356 between -0.66 and -1.04‰ , which is quite different from the situation at Tortosa, located a
357 few km upstream, where the Ca contents were almost the same.

358 All samples were undersaturated for gypsum and anhydrite, whereas for calcite,
359 aragonite and dolomite the water samples showed different saturation indices represented by
360 log SI (Table 2, calculated with PHREEQC, Parkhurst and Appelo, 1999; $\text{SI}=0$ is saturated,
361 $\text{SI}>0$ is supersaturated and $\text{SI}<0$ is undersaturated). The Ebro and tributary samples are
362 consistently supersaturated for calcite ($0.3<\text{SI}<0.9$ and $0.6<\text{SI}<1.0$), aragonite ($0.1<\text{SI}<0.7$
363 and $1.7<\text{SI}<2.7$) and dolomite ($0.9<\text{SI}<2.8$ and $0.4<\text{SI}<0.8$). During the survey at Amposta,
364 the samples varied significantly for calcite ($-2.3<\text{SI}<0.7$), aragonite ($-4.0<\text{SI}<2.0$) and
365 dolomite ($-2.5<\text{SI}<0.5$). The water samples were undersaturated for calcite and dolomite from
366 December to May and supersaturated between June and November (Table 2), and
367 undersaturated for aragonite from October to May and supersaturated from June to
368 September.



369

370 *Figure 3a, b. Variation of the Ca concentration (mg.L⁻¹) and δ⁴⁴Ca_{sw} value along the Ebro*
 371 *from headwaters (0 km) to outlet (550 km) for Ebro mainstream and tributary samples. The*
 372 *variations at the outlet (Amposta) are plotted with their sampling months; the red circle*
 373 *marks the sampling at Amposta at the same time as that of the Ebro mainstream.*
 374

375 5 – Discussion

376 5.1. Lithological control on major and trace elements

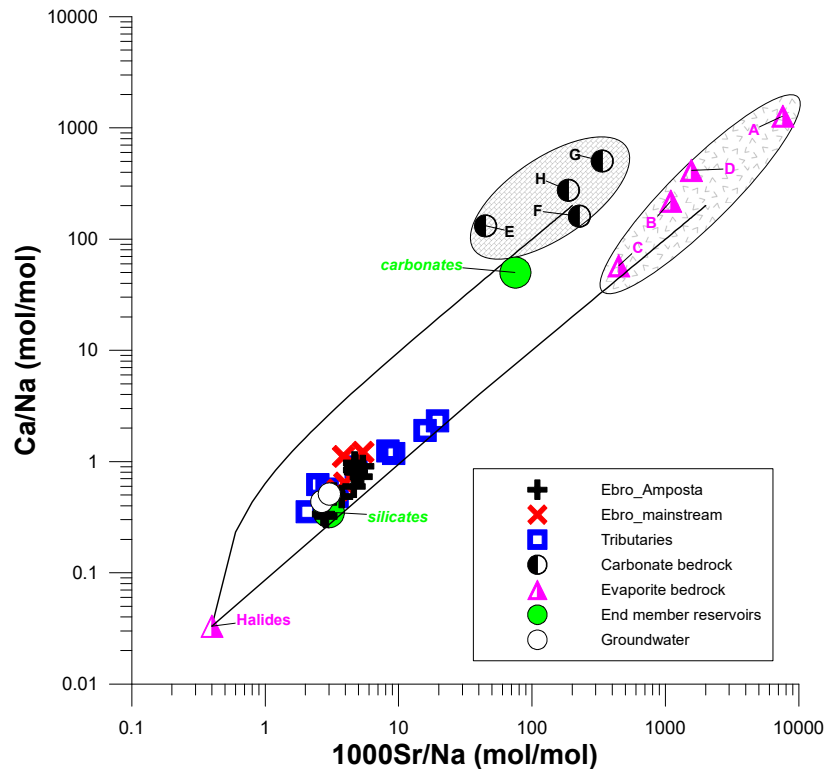
377 Négrel et al. (2007) and Petelet-Giraud and Négrel (2011) calculated export fluxes over more
 378 than 20 years, for dissolved- and solid-matter loads of the Ebro River Basin with data from
 379 the Confederación Hidrográfica del Ebro (<http://www.chebro.es/>). These calculations used
 380 TDS as the sum of ions, as well as co-variations between ions like Cl-Na, Ca-SO₄ or Ca-

381 HCO₃, and congruent weathering/dissolution reactions. At low concentrations, the Na/Cl
382 relationship illustrates the role of sea-salt cycling, while at higher concentrations the role of
383 the dissolution of Na-Cl-bearing rocks (e.g. evaporite) is predominant. The Ca contents are
384 counterbalanced by SO₄ and HCO₃, reflecting the dissolution of evaporites and carbonates.
385 Using only major ions, they illustrate the predominant role of export rates for evaporite-
386 gypsum (1.3x10⁶ to 3.5x10⁶ t.year⁻¹) and for carbonate (4.8x10⁵ to 1.8x10⁶ t.year⁻¹) at the last
387 (Tortosa) station and for the period 1981-2004. Using mean values, they found that the
388 dissolved-exportation rates at the outlet show that gypsum-derived weathering exceeds
389 carbonate-derived weathering by 1.5 times.

390 In addition, the discrimination of mixing in waters is well shown by cation values
391 (Négre^l et al., 1993; Gaillardet et al., 1999; Ruy et al., 2008). The simplest interaction
392 between carbonate, evaporite and water is the congruent dissolution of aragonite, calcite,
393 halite, gypsum and/or other minerals. Such dissolution releases Ca, Mg, Cl and SO₄, Na and
394 Sr into water. However, water/rock interaction with silicates causes an incongruent
395 dissolution of minerals, releasing a quasi-identical set of elements. This justifies the use of
396 cation values normalized to Na in a diagram like the Ca/Na vs. 1000Sr/Na (Fig. 4; Négre^l et
397 al., 1993; Gaillardet et al., 1999; 2003; Millot et al., 2003). The use of Na-normalized data (to
398 avoid concentration effects), reveals trends between the endmembers that can be considered
399 as mixing lines. Mixing of two solutions (a, b) with different sodium-normalized X/Na values
400 will lead to a mixed solution (i.e. “mix”) that will have an X/Na ratio given by Equation 2.

$$401 \quad X/Na_{\text{mix}} = m X/Na_a + (1 - m) X/Na_b \quad (\text{Eq. 2})$$

402 where X/Na a, b and ‘mix’ are sodium-normalized values for the solution mix from two
403 endmembers a and b, and m is the mixing proportion (Négre^l et al., 2010; Jacobson et al.,
404 2015).



405

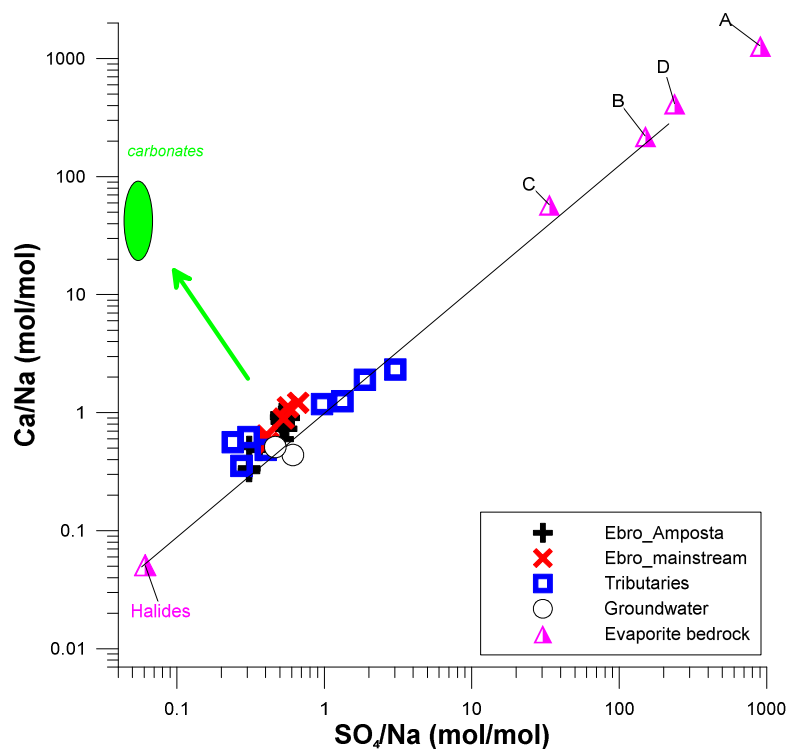
406 *Figure 4. General correlation between Ca/Na and Sr/Na values in samples from the Ebro*
 407 *basin (tributaries, mainstream, outlet survey, groundwater) and in regional bedrock. Solid*
 408 *lines show theoretical mixtures between halide endmembers (Soler et al., 2002), and average*
 409 *carbonate and evaporite (e.g. gypsum) endmember values deriving from different bedrocks*
 410 *collected in the Ebro basin. The carbonate and silicate endmember reservoirs are from*
 411 *Négreil et al. (1993) and Gaillardet et al. (1999).*

412

413

As many samples plot along the calculated mixing line on Figure 4 between the halide
 414 and anhydrite/gypsum endmembers, it is clear that the evaporite endmember reservoirs
 415 explain most of the data variability. The silicate endmember plots along this line and thus
 416 cannot discriminate silicate input (from tributaries draining the Pyrenees, such as the Segre).
 417 However, it is also clear that the halide and anhydrite/gypsum endmembers mixture cannot
 418 explain the entire data variability, and thus that other endmembers should be considered. The
 419 most obvious one is carbonate weathering represented by the second mixing line between the
 420 halide and carbonate endmembers for which the values derive from the different bedrocks
 421 collected in the Ebro basin. Some points are shifted from the first halide-anhydrite/gypsum
 422 mixing line toward the second halide-carbonate one, reflecting a much more ternary mixing
 423 rather than pure binary mixing.

424 Figure 5 illustrates Ca/Na vs. SO₄/Na, confirming the role of halide- and calcium-
 425 sulphate dissolution in controlling the dissolved load of the Ebro. Considering the larger
 426 rivers with evaporite bedrock in the basin, Gaillardet et al. (1999) stated that this endmember
 427 is certainly the most difficult to be constrained because of the diversity of salt-rock types.
 428 Figure 5 shows that evaporite endmembers explain most of the data variability, the carbonate
 429 endmember explaining the divergence of some points, mainly through Ca/Na variation.



430
 431 *Figure 5. General correlation between Ca/Na and SO₄/Na values the samples from the Ebro*
 432 *basin (tributaries, mainstream, outlet survey, groundwater) and in regional bedrock (only*
 433 *anhydrites/gypsum). Solid line shows theoretical mixtures between halide endmember (Soler*
 434 *et al., 2002), and an evaporite (e.g. gypsum) endmember (values from different bedrocks*
 435 *collected in the Ebro basin). The carbonate endmember reservoirs are estimated from Négrel*
 436 *et al. (1993) and Gaillardet et al. (1999).*
 437

438 **5.2 Sr source and contribution to water: Sr isotopes, bedrock and** 439 **mixing of different water sources**

440 Figure 6 shows the relationships between ⁸⁷Sr/⁸⁶Sr and Ca/Na. A similar scheme would be
 441 obtained by plotting Sr/Na instead of Ca/Na because of the good correlation between Ca/Na
 442 and Sr/Na values (Fig. 4). The relationships between several endmembers in the diagram

443 (Fig. 6) are represented by hyperbolae (Langmuir et al., 1978). The isotope systematics of
444 two-component mixtures, described by Faure (1986), were used for different cases (Hogan et
445 al., 2000; Négrel et al., 2010) and can be expressed as follows for Sr isotopes and Ca/Na
446 values (Equation 3). The mixed solution will have a $^{87}\text{Sr}/^{86}\text{Sr}$ (ISr in Eq. 3) of:

$$447 \quad \text{ISr}_{\text{mix}} = \left\{ \left(\frac{\text{Ca}/\text{Na}_a \times \text{ISr}_a \times m}{\text{Ca}/\text{Na}_{\text{mix}}} \right) + \left(\frac{\text{Ca}/\text{Na}_b \times \text{ISr}_b \times (1-m)}{\text{Ca}/\text{Na}_{\text{mix}}} \right) \right\} \text{ (Eq. 3)}$$

448 where Ca/Na_a , Ca/Na_b and $\text{Ca}/\text{Na}_{\text{mix}}$ are the values for a solution mix from two endmembers a
449 and b, ISr_a , ISr_b and ISr_{mix} are strontium isotope compositions, and m is the mixing
450 proportion.

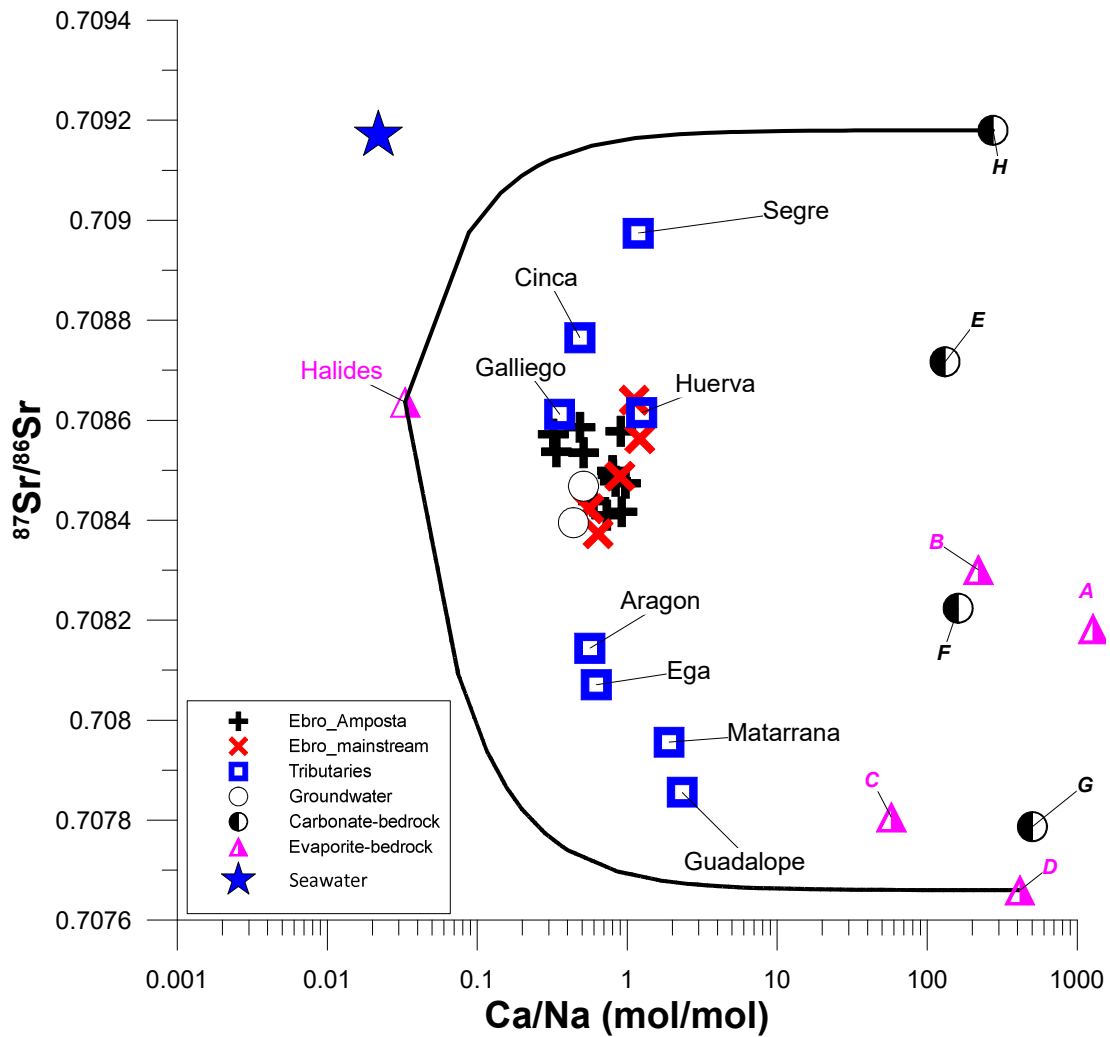
451 The $^{87}\text{Sr}/^{86}\text{Sr}$ vs. Ca/Na diagram shows that halide, anhydrite and carbonate
452 endmembers explain the data variability, and that silicate dissolution should not be considered
453 in the mixing scheme (low Ca/Na and high $^{87}\text{Sr}/^{86}\text{Sr}$ values). The earlier mentioned mixing
454 processes between carbonate and evaporite endmembers support the variability of all Ebro
455 samples.

456 The key question concerns the use of representative carbonate and evaporite
457 endmembers. The water draining carbonates and evaporites inherits the Sr-isotopic
458 composition of these rocks, as weathering of both is mostly congruent and no Rb can
459 influence the $^{87}\text{Sr}/^{86}\text{Sr}$ ratio of the water. Burke et al. (1982) documented the Sr-isotopic
460 composition of marine carbonates, evaporites, and phosphates and its secular variation, from
461 the Late Cambrian through the Holocene. However, for non-marine carbonate or evaporite
462 rocks, or diagenetically altered rocks, a larger degree of scatter is expected as the Sr-isotopic
463 composition depends on the Sr content of the water (Faure and Barrett, 1973). This led to a
464 larger $^{87}\text{Sr}/^{86}\text{Sr}$ ratio variation than the one observed for geologic time, i.e. with the lowest
465 values (~ 0.7068) occurring during the Jurassic and Late Permian, and a modern ratio of
466 0.70907. However, this is not shown in the carbonate and evaporite bedrock from the Ebro

467 basin, with ratios ranging from 0.70766 (sample D, Triassic anhydrite) to 0.70918 (sample H,
468 Oligocene carbonate facies), a variation of the same order as the marine variation. It is worth
469 noting that the strontium isotopic values of continental evaporites ($^{87}\text{Sr}/^{86}\text{Sr}=0.70788$ to
470 0.70793) from the continental Cameros Basin (Alonso-Azcárate et al., 2006) in the Iberian
471 ranges of northern Spain are identical to those we found.

472 The data scattering allowed defining two main relationships and the two extreme
473 calculated mixing lines showed two sample sets (Fig. 6). The first includes four of the Ebro
474 tributaries (Aragon, Ega, Matarrana and Guadalope) in a mixing scheme between high to low
475 Ca/Na values, the high Ca/Na endmember having the lowest $^{87}\text{Sr}/^{86}\text{Sr}$ ratio (sample D,
476 Triassic anhydrite). The mixing line for these rivers shows a larger role of evaporite
477 weathering in supplying Sr to the dissolved load, as only the Paleocene carbonate facies G can
478 be related to this mixing. The second mixing line mainly concerns the other four tributaries
479 (Huerva, Galliego, Cinca and Segre) in a scheme between high to low Ca/Na values, the high
480 Ca/Na endmember having the highest $^{87}\text{Sr}/^{86}\text{Sr}$ ratio (Oligocene carbonate facies H). For these
481 rivers, the mixing line highlights a shared role of evaporite (halides) and carbonate weathering
482 in the supply of Sr to the dissolved load. Several other mixing lines can be drawn between the
483 halide endmember and evaporites A, B plus carbonates E, F that cover all the other Ebro
484 River mainstream and outlet survey samples.

485



486

487 *Figure 6. $^{87}\text{Sr}/^{86}\text{Sr}$ vs. Ca/Na values (mol/mol) in Ebro basin bedrock samples (tributaries,*
 488 *mainstream, outlet survey, groundwater). Solid lines show theoretical mixtures between the*
 489 *halide endmembers (Soler et al., 2002) and extreme carbonate and evaporite samples of the*
 490 *different bedrocks collected in the Ebro basin.*

491

492 **5.3 Distribution of Ca isotopes in the water-rock interactions** 493 **system: mixing versus fractionation hypothesis**

494

495 As for Sr isotopes, Figure 7 shows the relationships between $\delta^{44}\text{Ca}_{\text{sw}}$ ratio and Ca/Na , where
 496 the mixtures between different endmembers are represented by hyperbolae (Langmuir et al.,
 497 1978). The isotope systematics of two-component mixtures, described for Sr isotopes in
 498 Equation 3, can be expressed similarly by $\delta^{44}\text{Ca}_{\text{sw}}$ replacing ISr . The $\delta^{44}\text{Ca}_{\text{sw}}$ value of
 499 anhydrite-gypsum bedrock ranges from -0.94 to -1.22‰ while that of carbonate bedrock
 500 ranges from -1.04 to -1.39‰. The two extreme values are for sample D (Triassic anhydrite)

501 and sample E from Triassic Muschelkalk. Two mixing lines between halides and the two
502 main bedrocks are shown on Fig. 7, the first with anhydrite and the second with carbonate
503 endmembers. Several Ebro basin samples are scattered between these mixing lines, mainly
504 along the one including halides and evaporite. For the Galliego, Aragon, Ega and Segre
505 tributaries, four samples collected along the Ebro mainstream and two collected at the Ebro
506 outlet can be explained by these mixing lines.

507 If the $\delta^{44}\text{Ca}_{\text{sw}}$ vs. Ca/Na diagram indicates that mixing between halide, anhydrite and
508 carbonate endmembers explains part of the data variability, several other samples do not
509 correspond to these processes, and geochemical processes like carbonate supersaturation must
510 be suspected for them (mainly Matarrana). Two mechanisms could enrich these river samples
511 in heavy Ca isotopes: uptake of light Ca by vegetation (Schmitt et al., 2012), or uptake of
512 light Ca by secondary calcite (Tang et al., 2008), the latter being the favoured hypothesis for
513 the Ebro basin. Removal of Ca through calcite precipitation would preferentially remove ^{40}Ca ,
514 leading to higher $\delta^{44}\text{Ca}_{\text{sw}}$ values for the theoretical mixtures (Lemarchand et al., 2004;
515 DePaolo, 2004; Tang et al., 2008). This can explain the higher $\delta^{44}\text{Ca}_{\text{sw}}$ values in river water
516 than expected from previously calculated mixtures, which are related to Ca-isotope
517 fractionation because of possible Ca loss, as the water is supersaturated with respect to calcite.

518 The transformation of soluble Ca to solid CaCO_3 involves a separation of aqueous and
519 solid phases for which an isotopic enrichment factor exists (Lemarchand et al., 2004;
520 Wiederhold, 2015). The extent of the reaction can be quantified—based on solid and
521 dissolved phases—from the heavy-isotope enrichment in the remaining reactant, using the
522 following equations for a Rayleigh-type fractionation model (Equation 4) and an equilibrium-
523 type fractionation model (Equation 5). This gives for Ca in water:

524
$$\delta^{44}\text{Ca}_{\text{river}} = \delta^{44}\text{Ca}_0 + 1000(\alpha-1) * \ln(f\text{Ca}) \quad \text{Eq. 4}$$

525
$$\delta^{44}\text{Ca}_{\text{river}} = \delta^{44}\text{Ca}_0 - 1000(\alpha-1) * (1-f\text{Ca}) \quad \text{Eq. 5}$$

526 where $\delta^{44}\text{Ca}_{\text{river}}$ is the measured ratio in the river water, $\delta^{44}\text{Ca}_0$ is the starting Ca-isotopic
527 composition of the river water (assumed to be close to that deriving from bedrock alteration in
528 the basin), α is the fractionation factor and $f\text{Ca}$ is the Ca fraction remaining in solution.
529 Rayleigh- or equilibrium-type fractionation models have been used for modelling Ca-isotope
530 fractionation in river basins (Tipper et al., 2006; Hindshaw et al., 2013), in aquifers (Jacobson
531 and Holmden, 2008), or in pore waters (Fantle and DePaolo, 2007).

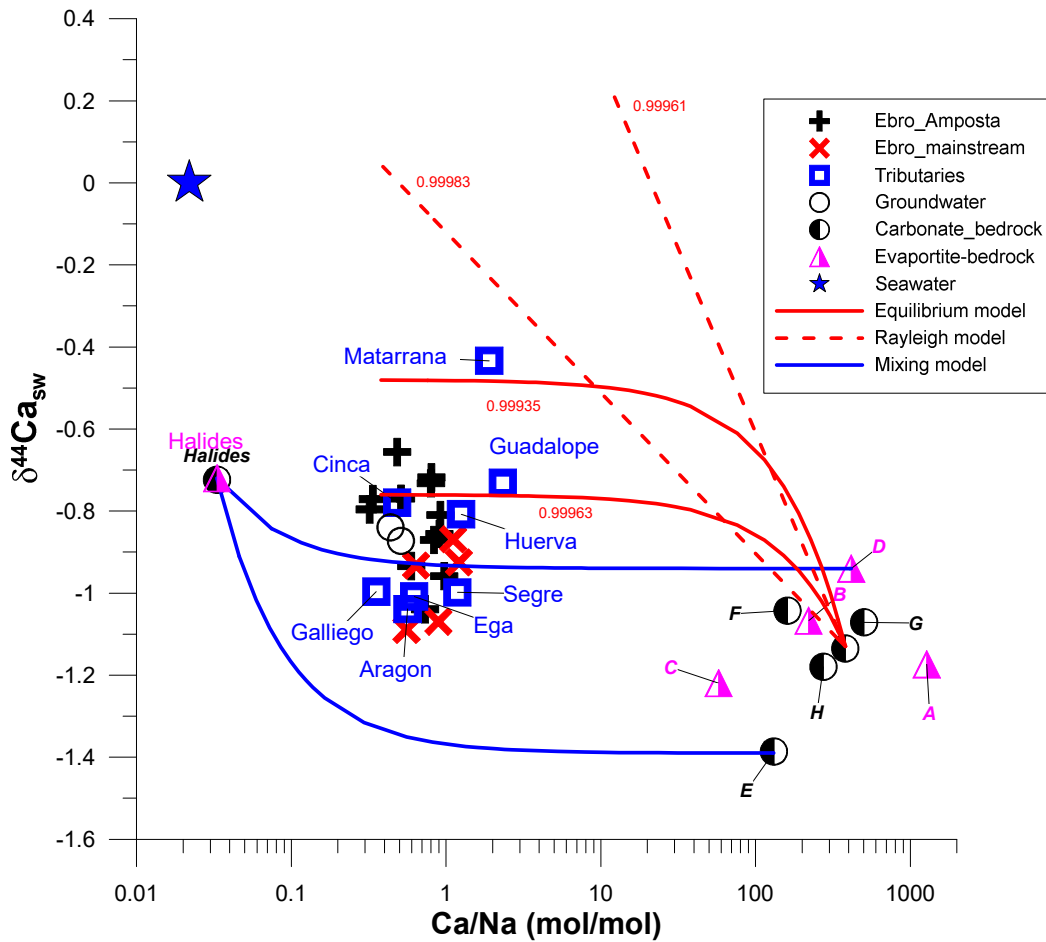
532 Rayleigh- and equilibrium-type models were calculated (Fig. 7). The Ca/Na ratio is
533 used to indicate Ca uptake into secondary phases. The Ca fraction remaining in solution was
534 estimated with Equation 6, equivalent to the calculation of Ca mobility relative to Na
535 (Hindshaw et al. 2013), as the release of Ca and Na from evaporite and carbonate bedrocks is
536 assumed to be congruent:

537
$$f\text{Ca} = (\text{Ca/Na})_{\text{river}} / (\text{Ca/Na})_{\text{bedrock}} \quad \text{Eq. 6}$$

538 A common $(\text{Ca/Na})_{\text{bedrock}}$ ratio of 2.87 was assumed for solving Equation 6, based on
539 the median of all evaporite and carbonate bedrocks, or 380 mol/mol. Associated with this
540 $(\text{Ca/Na})_{\text{bedrock}}$ value, a $\delta^{44}\text{Ca}_0$ ratio of -1.13‰ for evaporite and carbonate bedrocks was used in
541 Equation 6, based on the observed range in evaporite and carbonate bedrocks (-0.94 to -
542 1.39‰).

543 The range of fractionation factors classically defined as $\alpha = \delta^{44}\text{Ca}_{\text{mineral}} / \delta^{44}\text{Ca}_{\text{fluid}}$ used
544 for the Rayleigh fractionation model is $\alpha = 0.99961$ to 0.99983 and the equilibrium-type
545 fractionation model range is $\alpha = 0.99935$ to 0.99963 (Gussone et al., 2003, 2005; Lemarchand
546 et al., 2004; DePaolo, 2004; Fantle and DePaolo, 2007; Tang et al., 2008; Fantle, 2015). The
547 results of the two fractionation models are given on Figure 7. Regarding the tributaries, the
548 Guadalupe, Cinca and Huerva fit the equilibrium-type fractionation model and a fractionation
549 factor α of 0.99963. All samples collected along the Ebro mainstream and most of the samples
550 collected the Ebro outlet, as well the groundwater, can be explained by this fractionation line.

551 The use of a fractionation factor α of 0.99935 fits all samples except the Matarrana tributary.
 552 The Rayleigh-type fractionation model, regardless of the fractionation factor, always yields a
 553 higher $\delta^{44}\text{Ca}_{\text{sw}}$ than that observed in the basin. Evidence for secondary mineral precipitation
 554 influencing the $\delta^{44}\text{Ca}$ values is shown by the fractionation models, the saturation index data
 555 fitting the equilibrium-type fractionation model.



556

557 *Figure 7. $\delta^{44}\text{Ca}_{\text{sw}}$ vs. Ca/Na values (mol/mol) in Ebro basin bedrock samples (tributaries,*
 558 *mainstream, outlet survey, groundwater). The blue solid lines show theoretical mixtures*
 559 *between the halide endmembers (Soler et al., 2002), and extreme carbonate and evaporite*
 560 *samples collected in the Ebro basin. Solid red lines represent the equilibrium-type*
 561 *fractionation model with a fractionation factor α in the range 0.99935 to 0.99963 and dashed*
 562 *red lines represent the Rayleigh-type fractionation model with a fractionation factor α in the*
 563 *range 0.99961 to 0.99983.*

564

565 However, there is no simple relationship between $\delta^{44}\text{Ca}_{\text{sw}}$ values and the calcite
566 saturation index (Fig. 8), the latter being indicative of carbonate precipitation and affecting
567 the variability of $\delta^{44}\text{Ca}_{\text{sw}}$ values. Two main features can be seen on Figure 8.

568 The first feature groups the tributary, Ebro and groundwater samples, with a notable
569 variability in the riverine $\delta^{44}\text{Ca}_{\text{sw}}$ values that range between -0.43 and 1.09‰, a $\text{SI}_{\text{calcite}}$
570 ranging between 0.3 and 0.99 for tributary and Ebro waters, and a 0.96-1.15 range for
571 groundwater. The two extreme $\delta^{44}\text{Ca}_{\text{sw}}$ values are for Aragon (-1.04‰) and Matarrana (-
572 0.43‰), with a small $\text{SI}_{\text{calcite}}$ range (0.71 to 0.82) showing a higher variability of $\delta^{44}\text{Ca}_{\text{sw}}$
573 values compared to those of the saturation index. We then compared the $\delta^{44}\text{Ca}_{\text{sw}}$ values,
574 $\text{SI}_{\text{calcite}}$ and the distance of the sample from the source (from 100 km up to 450 km) for the
575 Ebro mainstream. This showed that both $\text{SI}_{\text{calcite}}$ and $\delta^{44}\text{Ca}_{\text{sw}}$ values show slight variations,
576 between 0.57 and 0.99 for $\text{SI}_{\text{calcite}}$ and between -0.87 and -1.09‰ for $\delta^{44}\text{Ca}_{\text{sw}}$, but where the
577 $\text{SI}_{\text{calcite}}$ variation is uncorrelated with the distance from the river source, the $\delta^{44}\text{Ca}_{\text{sw}}$ values
578 decrease with an increasing distance from the source.

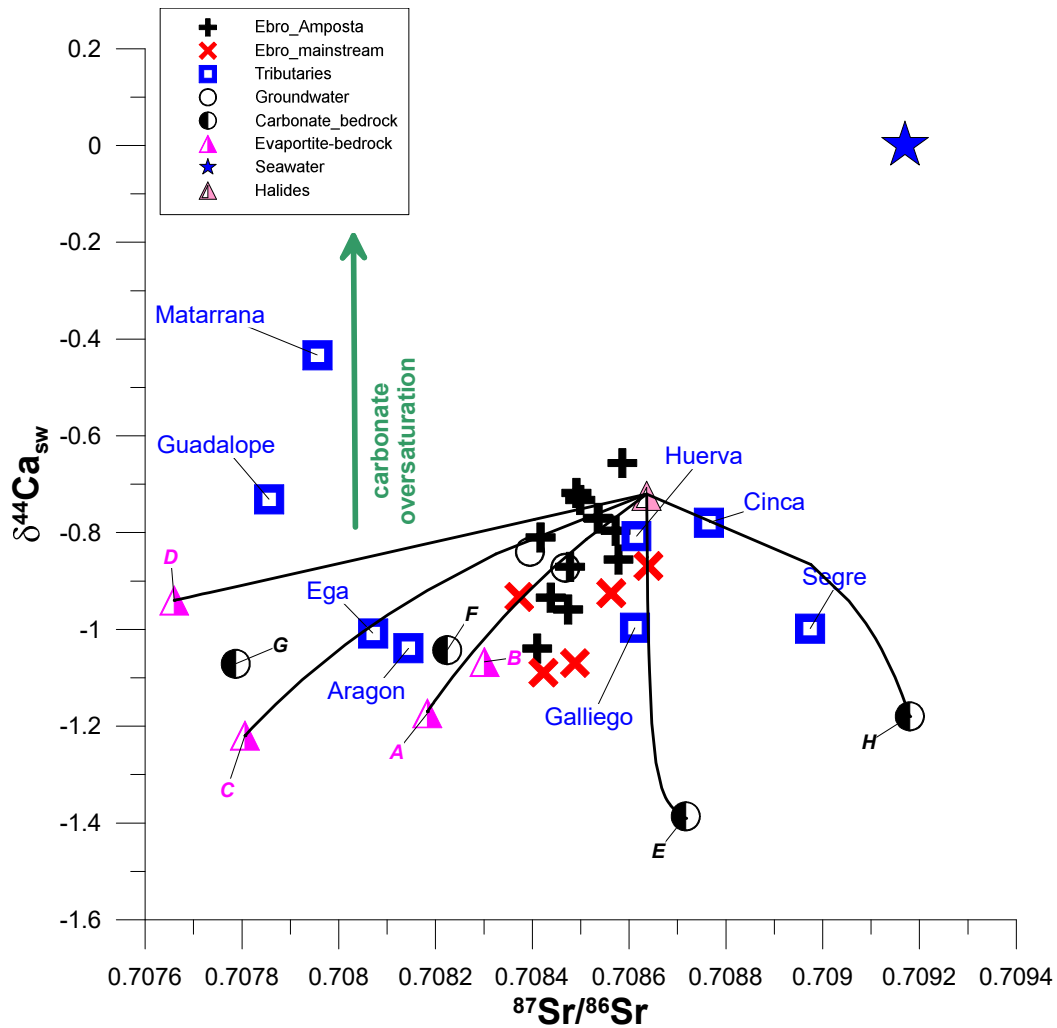
579 The second feature only concerns the Ebro at the Amposta outlet. Here, with a strong
580 temporal variability for both $\text{SI}_{\text{calcite}}$ and $\delta^{44}\text{Ca}_{\text{sw}}$ parameters (Fig. 8), the $\text{SI}_{\text{calcite}}$ values range
581 from <0 and undersaturated (-2.31) in January, to >0 and supersaturated (0.66) in August.
582 This will be discussed in the following section.

598 isotopes—robust fluid tracers—also for tracing sources (Subias et al., 1998; Schmitt et al.,
599 2003a; Soudry et al., 2004). As halides contain little Ca, the comparison of $\delta^{44}\text{Ca}$ and
600 $^{87}\text{Sr}/^{86}\text{Sr}$ values provided additional information on the role of anhydrites and carbonates in
601 identifying the provenance of the waters in the Ebro and its tributaries.

602 Figure 9 shows the relationships between $\delta^{44}\text{Ca}_{\text{sw}}$ values and $^{87}\text{Sr}/^{86}\text{Sr}$ values; mixtures
603 between different endmembers are represented by curves calculated with Equation 3 for Sr
604 isotopes, and adapted to Ca-isotope mixtures, using $\delta^{44}\text{Ca}_{\text{sw}}$ instead of ISr (Langmuir et al.,
605 1978). Considering only mixing processes, all samples are explained by mixing lines with
606 different endmembers. Mixtures between halides and C (Eocene anhydrite), D (Triassic
607 anhydrite) and A (Miocene gypsum) evaporites, or H (Oligocene) and E (Triassic
608 Muschelkalk) carbonates, explain most water-sample results except those from the
609 Guadalope, Matarrana, Segre and Cinca tributaries, and two Ebro outlet samples where Ca-
610 isotope fractionation is the main process explaining a value shift up to the mixing lines.

611 Tipper et al. (2006, 2010) measured Ca-isotope values of numerous rivers—including
612 seventeen of the World’s largest—that provide more than one third of the total Ca input into
613 the oceans today. Compiling these data provides a view of the drainage of a wide range of
614 tectonic, climatic and geological environments.

615



616

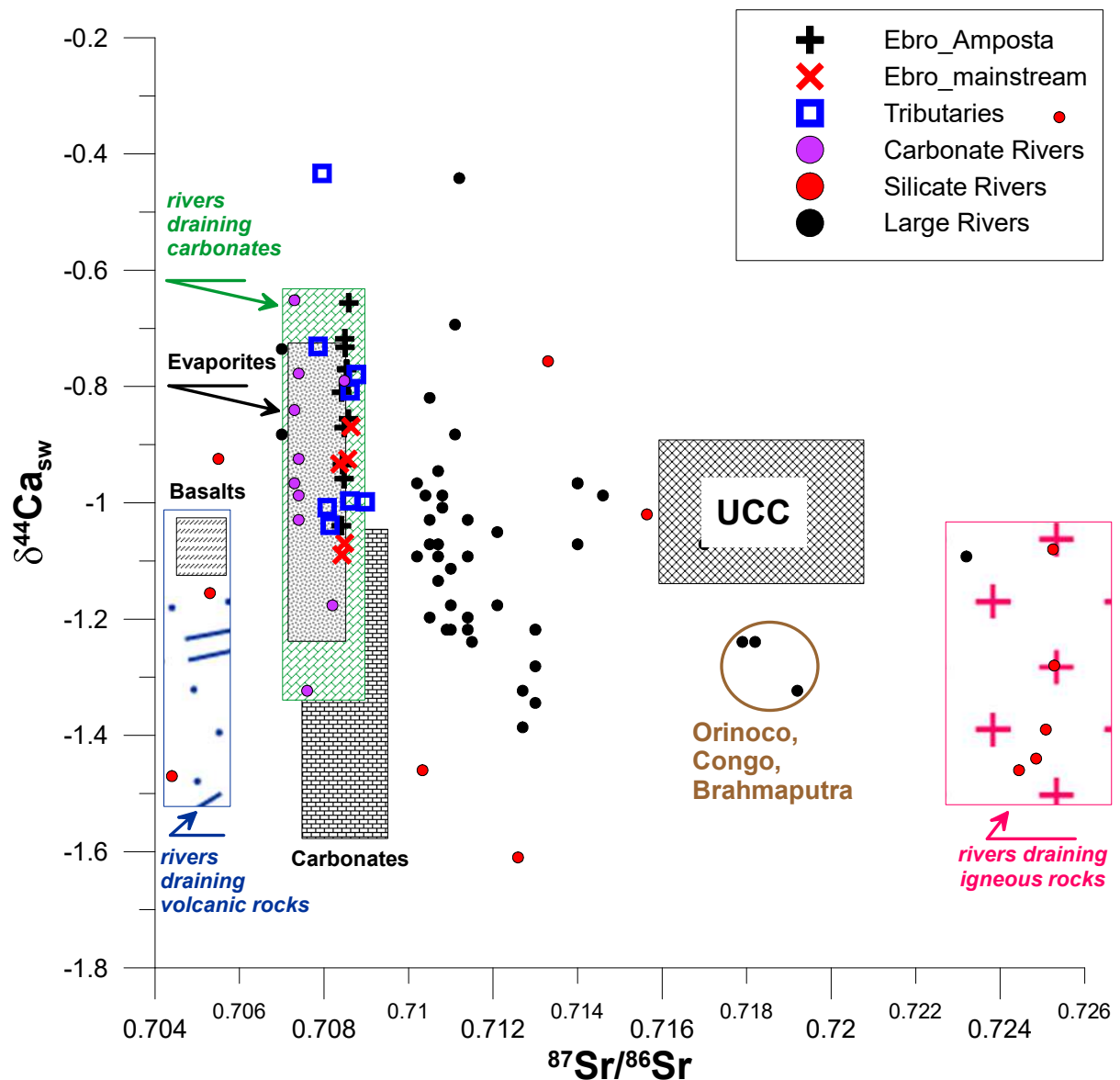
617 *Figure 9. $^{87}\text{Sr}/^{86}\text{Sr}$ ratios vs. $\delta^{44}\text{Ca}_{\text{sw}}$ values in the Ebro basin samples (tributaries,*
 618 *mainstream, outlet survey, groundwater) from regional bedrock. Solid lines show theoretical*
 619 *mixtures between halide endmembers (Soler et al., 2002), and extreme carbonate and*
 620 *evaporite bedrock samples.*

621

622

623 Figure 10 shows the global scheme using the data from Tipper et al. (2006, 2010). In
 624 this graph are indicated the Upper Continental Crust, rivers draining igneous rocks, rivers
 625 draining basaltic rocks, mean basaltic and carbonate rocks and the large rivers. Within the
 626 field of rivers draining carbonate rocks, we have included the data from the Ebro basin. These
 627 fit well, with the exception of the Matarrana tributary that has a higher $\delta^{44}\text{Ca}_{\text{sw}}$ value. Tipper
 628 et al. (2010) argued that the Ca-isotope compositions of rivers draining carbonate are
 629 consistent with the Ca-isotope data of such rock, and that more systematic work on Ca-
 isotopes in rivers draining limestone is required. Our data from the Ebro basin (Fig. 8) show

630 that Ca isotopes in rivers draining carbonate rock may not be in equilibrium with the bedrock
 631 values because of possible Ca precipitation as calcite-aragonite and the associated
 632 fractionation of the $\delta^{44}\text{Ca}_{\text{sw}}$ values, as discussed above. The data obtained on the Ebro River
 633 basin complement well the Fig. 10 by adding data on rivers draining carbonate and new data
 634 on rivers draining evaporates which did not exist until now.
 635



636
 637 *Figure 10. $^{87}\text{Sr}/^{86}\text{Sr}$ values vs. $\delta^{44}\text{Ca}_{\text{sw}}$ values in Ebro basin (tributaries, mainstream, outlet*
 638 *survey) samples and in the largest rivers in the World and rock endmembers (Tipper et al.,*
 639 *2010, this study). Carbonate rivers, silicate rivers and large rivers correspond to the*
 640 *classification of Tipper et al. (2006, 2010).*
 641

642 **5.5 A temporal vision of the Ebro basin: Sr- and Ca-isotope**
643 **variations**

644
645 The Ebro surface waters collected at different stages of the water cycle at the Amposta station
646 display a similar behaviour for Ca and Sr concentrations (as well as for other elements like Cl
647 or Na). The Ca and Sr concentrations generally decrease as the discharge increases (Fig. 11a,
648 b), with higher concentrations during autumn and winter and lower concentrations in
649 springtime. Note the different behaviour for three samples (December, January and March).
650 These samples differ from the general trend more by an increase in river flow than by Ca- or
651 Sr-concentration differences that are due to water releases from reservoirs (Batalla et al.,
652 2004). As shown by Prats et al. (2010), the Ebro basin is typical for its reduced flow in
653 autumn and winter because of dam storage and its increased flow due to summer releases for
654 irrigation that increase base flow above natural levels.

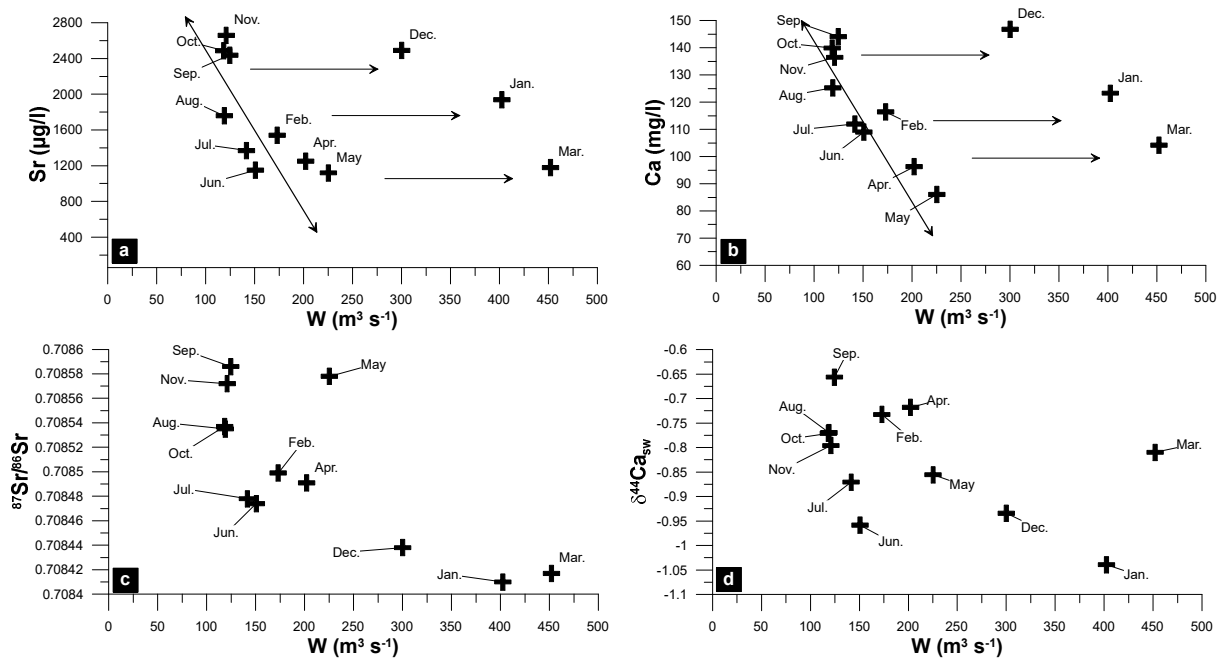
655 In the Ebro basin, the impounded water is used for hydropower generation, irrigation,
656 cooling water for nuclear power plants, and for industry and domestic uses. As usual in
657 impounded basins, when the reservoirs have stored sufficient water during autumn and winter
658 to ensure supply during the period of high demand in late spring and summer, water is
659 released according to surplus inflow. However, an increase in Ebro discharge was observed
660 for periods when decrease is more expected; this may correspond to a release of water from
661 the major Flix reservoir in the downstream part of the basin, to adapt its filling level to its
662 optimal use.

663 The $^{87}\text{Sr}/^{86}\text{Sr}$ ratios and $\delta^{44}\text{Ca}_{\text{sw}}$ values *versus* Ebro River discharge (Fig. 11c, d) show
664 a similar pattern, but with higher and lower values that do not fully correspond to the same
665 periods. The highest values for Sr isotopes occurred in September and November, while the
666 ones for Ca isotopes were observed for September, November having a lower value. The
667 lowest Sr-isotope values occurred in January and March, though for Ca isotopes the lowest

668 values were only observed in January, March having a higher value. Note that the three points
 669 with a marked shift in Sr concentration vs. discharge (December, January and March) had
 670 lower Sr-isotopic ratios as the discharge increased. The $\delta^{44}\text{Ca}_{\text{sw}}$ values were identical for
 671 November and March samples ($\delta^{44}\text{Ca}_{\text{sw}}=-0.81$ and -0.80‰ ; respectively), but the $\text{SI}_{\text{calcite}}$
 672 fluctuated between -1.26 in March (undersaturated) and 0.06 (saturated) in November,
 673 agreeing with the lack of relationship locally observed between Ca-isotope fractionation and
 674 calcite-aragonite saturation of the waters (Tipper et al. 2006; 2010). Changes in discharge
 675 could be one reason for the isotopic variations. In studies from rivers with large seasonal
 676 discharge variations, it was shown that, during high-discharge periods, Ca-isotopic values are
 677 closer to bedrock values than during low discharge (op. cit.).

678

679



680

681 *Figure 11a-d. Sr (µg L⁻¹), Ca concentration (mg L⁻¹), ⁸⁷Sr/⁸⁶Sr ratios and δ⁴⁴Ca_{sw} values*
 682 *versus Ebro River discharge at the Amposta station for each monthly sample.*

683

684 In Figure 8, a trend marked by a bell curve is highlighted by samples of Ebro surface
685 waters collected at different stages of the water cycle at the Amposta station. The $\delta^{44}\text{Ca}_{\text{sw}}$
686 values increased as the $\text{SI}_{\text{calcite}}$ increased between January and May, even though the waters
687 were undersaturated, but the highest $\delta^{44}\text{Ca}_{\text{sw}}$ values were for April and not May. The $\delta^{44}\text{Ca}_{\text{sw}}$
688 values decreased as the $\text{SI}_{\text{calcite}}$ decreased between June and November, but the lowest
689 $\delta^{44}\text{Ca}_{\text{sw}}$ values (and highest $\text{SI}_{\text{calcite}}$) occurred in June. An interesting point is the large
690 difference between the $\delta^{44}\text{Ca}_{\text{sw}}$ value of around -0.72‰ sampled at Amposta at the same time
691 as that sampled in the Ebro at Tortosa, a few km upstream (-1.07‰). This large variation also
692 existed for $\text{SI}_{\text{calcite}}$ (-0.96 in Amposta against 0.79 in Tortosa), but, surprisingly, the Ca
693 contents were similar in both sites. This apparent anomaly may have been caused by the Flix
694 reservoir releasing water undersaturated in calcium (Négrel et al., 2016).

695 In terms of output to the sea, the mean $\delta^{44}\text{Ca}_{\text{sw}}$ value of the Ebro River at Amposta is -
696 $0.83\text{‰}\pm 0.11$ ($n=12$), similar to the mean value of the tributaries ($-0.85\text{‰}\pm 0.12$; $n=8$). The
697 mean Ebro value is similar to the $\delta^{44}\text{Ca}_{\text{sw}}$ one given by Tipper et al. (2010) in their study of
698 the oceanic Ca budget ($-0.96\text{‰}\pm 0.22$; $n=13$). The only large rivers analysed for Ca-isotope
699 ratios to constrain the isotopic mass balance were the Seine and Rhine rivers. The average
700 riverine value of Ca isotopes (Tipper et al., 2010), in view of the uncertainty of the main Ca
701 output to the oceans, is not modified when incorporating a value like the one obtained for the
702 Ebro River.

703 **6 – Conclusions**

704 Investigations of surface- and groundwaters from the Ebro River Basin, the largest river of the
705 Iberian Peninsula and one of the largest in the Mediterranean region, defined a detailed
706 behaviour of Sr and Ca isotopes in the weathering environment at the catchment scale. In the

707 limestone-evaporite dominated rivers from the Ebro basin (Spain) with its reduced vegetation,
708 river waters are isotopically heavier than limestone bedrock for $\delta^{44}\text{Ca}_{\text{sw}}$ by up to 0.5‰.

709 Comparing Ca and SO_4 values (normalized to Na and Sr) with Ca-isotope values,
710 showed the role of anhydrite/halide weathering for some tributaries (Guadalope, Matarrana,
711 Aragon, Ega), the role of carbonate/halide weathering being predominant for the others
712 (Gallego, Cinca, Segre), the Ebro mainstream being a mix of both. This can be modelled for
713 Sr isotopes by a mixture between carbonate and evaporite endmembers, thus covering the
714 variability of all samples from the Ebro basin.

715 For Ca isotopes, we compared the mixing model between the bedrock endmembers,
716 considering the uptake of Ca into secondary phases, the equilibrium-type fractionation model
717 with a fractionation factor α ranging from 0.99935 to 0.99963, and the Rayleigh-type
718 fractionation model with α in the range 0.99961 to 0.99983. Evidence that secondary-mineral
719 precipitation influences $\delta^{44}\text{Ca}$ values is shown by the fractionation models, but the data fit
720 well with the equilibrium-type fractionation model as well as with saturation indices.

721 We compared the Ca-isotope values of the Ebro basin with a global set of river data
722 from the literature (Tipper et al., 2006, 2010), including the largest rivers on Earth, and with
723 different lithotectonic and climatic settings. We plotted our Ebro basin data on the field of
724 rivers draining carbonate rock, which fitted the field defined in the literature except for one
725 tributary (Matarrana) with a high $\delta^{44}\text{Ca}_{\text{sw}}$ value. We demonstrated that Ca isotopes in river
726 waters draining limestone can be in disequilibrium with the bedrock values, because of Ca
727 precipitation as calcite-aragonite and the associated fractionation of $\delta^{44}\text{Ca}_{\text{sw}}$ values.

728 Throughout the annual hydrological cycle of the Ebro River at the outlet, Ca-isotope
729 values and mineral-saturation indices SI in the dissolved load define a trend marked by a bell
730 curve. The $\delta^{44}\text{Ca}_{\text{sw}}$ values increase as the $\text{SI}_{\text{calcite}}$ increases between January and May, even if
731 the water is undersaturated in calcium, and decrease as the $\text{SI}_{\text{calcite}}$ decreases between June and

732 November. This may well be due to releases of Flix-reservoir water with various saturation
733 indices, depending upon its operation in terms of water storage-destocking.

734

735 **Acknowledgements**

736 This work was funded by the BRGM Research Division and by the European Union (integrated
737 project AquaTerra, Project GOCE 505428) under the thematic priority “Sustainable Development,
738 Global Change and Ecosystems (FP6) Water Cycle and Soil Related Aspects”. The views expressed
739 are purely those of the writers and may not under any circumstances be regarded as stating an official
740 position of the European Commission.

741 We thank M. Brach for collecting the samples along the Ebro basin and D. Barcelo’s team (CSIC
742 Barcelona, Spain) for providing assistance in sample collection. We are grateful to Dr. Laura Rosell,
743 Dr. Federico Orti and Dr. Lluís Cabrera for providing the bedrock samples. The authors acknowledge
744 the support on the information received from the Agencia Catalana de l’Aigua and the Confederación
745 Hidrográfica del Ebro (CHE). We are grateful to Dr. H.M. Kluijver for proofreading and editing the
746 English text. In memory of our wonderful colleague and friend, Dr. Thomas (Tom) Bullen, 1951-2018
747 (Shouakar-Stash et al., 2018) with whom we started the calcium adventure in our labs a few years ago.

748 **References**

- 749 Åberg, G. 1995. The use of natural strontium isotopes as tracers in environmental studies. *Water, Air,*
750 *Soil Poll.* 79, 309-322.
- 751 Alonso-Azcárate, J., Bottrell, S.H., Mas J.R., 2006. Synsedimentary versus metamorphic control of S,
752 O and Sr isotopic compositions in gypsum evaporites from the Cameros Basin, Spain. *Chem. Geol.*
753 234, 46–57.
- 754 Amini, M., Eisenhauer, A., Böhm, F., Fietzke, J., Bach, W., Garbe-Schönberg, D., Rosner, M., Bock,
755 B., Lackschewitz, K.S., Hauff, F., 2008. Calcium isotope ($\delta^{44/40}\text{Ca}$) fractionation along
756 hydrothermal pathways, Logatchev field (Mid-Atlantic Ridge, 14°45’N). *Geochim. Cosmochim.*
757 *Acta* 72, 4107-4122.
- 758 Batalla, R.J., Gomez, C.M., Kondolf, G.M., 2004. Reservoir-induced hydrological changes in the Ebro
759 River Basin, NE Spain. *J. Hydrol.* 290, 117–136.
- 760 Blättler, C.L., Higgins, J.A., 2014. Calcium isotopes in evaporites record variations in Phanerozoic
761 seawater SO_4 and Ca. *Geol.* 42, 711-714.

762 Blättler, C.L., Jenkyns, H.C., Reynard, L.M., Henderson, G.M., 2011. Significant increases in global
763 weathering during Oceanic Anoxic Events 1a and 2 indicated by calcium isotopes. *Earth Planet.*
764 *Sci. Lett.* 309, 77-88.

765 Bradbury, H.J., Halloran, K.H., Lin, C.Y., Turchyn, A.V., 2020. Calcium isotope fractionation during
766 microbially induced carbonate mineral precipitation. *Geochim. Cosmochim. Acta* 277, 37-51.

767 Brazier, J.M., Suan, G., Tacail, T., Simon, L., Martin, J.E., Mattioli, E., Balter, V., 2015. Calcium
768 isotope evidence for dramatic increase of continental weathering during the Toarcian oceanic
769 anoxic event (Early Jurassic). *Earth Planet. Sci. Lett.* 411, 164-176.

770 Brazier, J.M., Schmitt, A.D., Gangloff, S., Pelt, E., Chabaux, F., Tertre, E., 2019. Calcium isotopic
771 fractionation during adsorption onto and desorption from soil phyllosilicates (kaolinite,
772 montmorillonite and muscovite). *Geochim. Cosmochim. Acta* 250, 324-347.

773 Burke, W.H., Denison, R.E., Hetherington, E.A., Koepnick, R.B., Nelson, H.F., Otto, J.B., 1982.
774 Variation of seawater $^{87}\text{Sr}/^{86}\text{Sr}$ throughout Phanerozoic time. *Geol.* 10, 516-519.

775 Castillo Herrador, F., 1974. Le Trias évaporitique des bassins de la vallée de l'Ebre et de Cuenca. *Bull.*
776 *Soc. Géol. France* 7, 666-676.

777 Chabaux, F., Riotte, J., Schmitt, A.D., Carignan, J., Herckes, P., Pierret, M.C., Wortham, H., 2005.
778 Variations of U and Sr isotope values in Alsace and Luxembourg rain waters: origin and
779 hydrogeochemical implications. *C.R. Geoscience* 337, 1447-1456.

780 Chang, V.T.C., Williams, R.J.P., Makishima, A., Belshaw, N.S., O'Nions, R.K., 2004. Mg and Ca
781 isotope fractionation during CaCO_3 biomineralisation. *Biochem. Biophys. Res. Comm.* 323, 79-85.

782 Chen, B.B., Li, S.L., von Strandmann, P.A.P., Sun, J., Zhong, J., Li, C., Ma, T.T., Xu, S., Liu, C.Q.,
783 2020a. Ca isotope constraints on chemical weathering processes: Evidence from headwater in the
784 Changjiang River, China. *Chem. Geol.* 531, 119341.

785 Chen, C., Ciazela, J., Li, W., Dai, W., Wang, Z., Foley, S.F., Li, M., Hu, Z., Liu, Y., 2020b. Calcium
786 isotopic compositions of oceanic crust at various spreading rates. *Geochim. Cosmochim. Acta* 278,
787 272-288.

788 Cenko-Tok, B., Chabaux, F., Lemarchand, D., Schmitt, A.D., Pierret, M.C., Viville, D., Bagard, M.-L.,
789 Stille, P., 2009. The impact of water-rock interaction and vegetation on calcium isotope
790 fractionation in soil-and stream waters of a small, forested catchment (the Strengbach case).
791 *Geochim. Cosmochim. Acta* 73, 2215-2228.

792 Coplen, T.B., Hopple, J.A., Böhlke, J.K., Peiser, H.S., Rieder, S.E., Krouse, H.R., Rosman, K.J.R.,
793 Ding, T., Vocke, R.D. Jr., Révész, K.M., Lamberty, A., Taylor, P., De Bièvre, P., 2002.
794 Compilation of minimum and maximum isotope values of selected elements in naturally occurring
795 terrestrial materials and reagents. U.S. Geological Survey, Water-Resources Investigations, Report
796 01-4222.

797 Cruzado, A., Zoila Velasquez, Z., del Carmen Perez, M., Bahamon, N., Grimaldo N.S., Ridolfi, F.,
798 2002. Nutrient fluxes from the Ebro River and subsequent across-shelf dispersion. *Continental Shelf*
799 *Res.* 22, 349–360.

800 DePaolo, D.J., 2004. Calcium isotope variations produced by biological, kinetic, radiogenic, and
801 nucleosynthetic processes. In: Johnson, C.M., Beard, B.L., Albarede, F. (Eds.), *Geochemistry of*
802 *Non-traditional Stable Isotopes. Reviews in Mineralogy.* Mineral. Soc. of America, Washington
803 DC, pp. 255–288.

804 De La Rocha, C.L., DePaolo, D.J., 2000. Isotopic evidence for variations in the marine calcium cycle
805 over the Cenozoic. *Sci.* 289, 1176–1178.

806 Du Vivier, A.D., Jacobson, A.D., Lehn, G.O., Selby, D., Hurtgen, M.T., Sageman, B.B., 2015. Ca
807 isotope stratigraphy across the Cenomanian–Turonian OAE 2: Links between volcanism, seawater
808 geochemistry, and the carbonate fractionation factor. *Earth Planet. Sci. Lett.* 416, 121–131.

809 Elorza, M.G., Santolalla, F.G., 1998. Geomorphology of the Tertiary gypsum formations in the Ebro
810 Depression (Spain). *Geoderma* 87, 1–29.

811 English, N.B., Quade, J., DeCelles, P.G., Garzzone, C.N., 2000. Geologic control of Sr and major
812 element chemistry in Himalayan Rivers, Nepal. *Geochim. Cosmochim. Acta* 64, 2549–2566.

813 Fantle, M.S., 2010. Evaluating the Ca isotope proxy. *Amer. J. Sci.* 310(3), 194–230.

814 Fantle, M.S., 2015. Calcium isotopic evidence for rapid recrystallization of bulk marine carbonates
815 and implications for geochemical proxies. *Geochim. Cosmochim. Acta* 148, 378–401.
816 <http://dx.doi.org/10.1016/j.gca.2014.10.005>.

817 Fantle, M.S., DePaolo, D.J., 2005. Variations in the marine Ca cycle over the past 20 million years.
818 *Earth Planet. Sci. Lett.* 237, 102–117.

819 Fantle, M.S., DePaolo, D.J., 2007. Ca isotopes in carbonate sediment and pore fluid from ODP Site
820 807A: the Ca²⁺(aq)–calcite equilibrium fractionation factor and calcite recrystallization rates in
821 Pleistocene sediments. *Geochim. Cosmochim. Acta* 71, 2524–2546.

822 Fantle, M.S., Bullen, T.D., 2009. Essentials of iron, chromium, and calcium isotope analysis of natural
823 materials by thermal ionization mass spectrometry. *Chem. Geol.* 258(1–2), 50–64.

824 Fantle, M.S., Tipper, E.T., 2014. Calcium isotopes in the global biogeochemical Ca cycle:
825 implications for development of a Ca isotope proxy. *Earth Sci. Rev.* 129, 148–177.
826 <http://dx.doi.org/10.1016/j.earscirev.2013.10.004>.

827 Faure, G., Barrett, P. J. 1973. Strontium isotope compositions of non-marine carbonate rocks from the
828 Beacon Supergroup of the Transantarctic Mountains. *J. Sed. Res.* 43, 447–457.

829 Faure, G., 1986. *Principles of Isotope Geology.* John Wiley and Sons.

830 Gaillardet, J., Dupré, B., Louvat, P., Allègre, C.J., 1999. Global silicate weathering and CO₂
831 consumption rates deduced from the chemistry of large rivers. *Chem. Geol.* 159, 3–30.

832 Gaillardet, J., Millot, R., Dupré, B., 2003. Chemical denudation rates of the western Canadian
833 orogenic belt: the Stikine terrane. *Chem. Geol.* 201, 257–279.

834 García, M.A., Moreno, M.C., 2000. Los aprovechamientos en la Cuenca del Ebro: Afección en el
835 regimen hidrológico fluvial, Internal Technical Report no. 2000-PH-24.1, Confederación
836 Hidrográfica del Ebro, Zaragoza, 83pp.

837 García-Ruiz, J.M., López-Moreno, J.I., Vicente-Serrano, S.M., Lasanta-Martínez, T., Beguería, S.,
838 2011. Mediterranean water resources in a global change scenario. *Earth-Science Reviews* 105,
839 121–139.

840 Gigoux, M., Négrel, Ph., Guerrot, C., Brigaud, B., Delpéch, G., Pagel, M., Augé, T., 2015. $\delta^{44}\text{Ca}$ of
841 stratabound fluorite deposits in Burgundy (France): tracing fluid origin and/or fractionation
842 processes. *Procedia Earth and Planetary Science* 13, 129-133.

843 Goldstein, S.J., Jacobsen, S.B., 1987. The Nd and Sr isotopic systematics of river-water dissolved
844 material: Implications for the sources of Nd and Sr in seawater. *Chem. Geol.: Isotope Geoscience*
845 section, 66, 245-272.

846 Griffith, E.M., Schmitt, A.D., Andrews, M.G., Fantle, M.S., 2020. Elucidating modern geochemical
847 cycles at local, regional, and global scales using calcium isotopes. *Chem. Geol.* 534, 119445.

848 Griffith, E.M., Fantle, M.S., 2020. Introduction to calcium isotope geochemistry: Past lessons and
849 future directions. *Chem. Geol.* 537, 119470.

850 Grosbois, C., Négrel, Ph., Fouillac, C., Grimaud, D., 2000. Dissolved load of the Loire River:
851 chemical and isotopic characterization. *Chem. Geol.* 170, 179-201.

852 Guillen, J., Palanques, A., 1992. Sediment Dynamics and Hydrodynamics in the Lower Course of a
853 River Highly Regulated by Dams: the Ebro River. *Sedimentology* 39, 567–579.

854 Gussone, N., Eisenhauer, A., Heuser, A., Dietzel, M., Bock, B., Böhm, F., Spero, H.J., Lea, D.W.,
855 Bijma, J., Nägler, T.F., 2003. Model for kinetic effects on calcium isotope fractionation ($\delta^{44}\text{Ca}$) in
856 inorganic aragonite and cultured planktonic foraminifera. *Geochim. Cosmochim. Acta* 67, 1375–
857 1382. [http://dx.doi.org/10.1016/S0016-7037\(02\)01296-6](http://dx.doi.org/10.1016/S0016-7037(02)01296-6).

858 Gussone, N., Böhm, F., Eisenhauer, A., Dietzel, M., Heuser, A., Teichert, B.M.A., Reitner, J.,
859 Wörheide, G., Dullo, W.C., 2005. Calcium isotope fractionation in calcite and aragonite. *Geochim.*
860 *Cosmochim. Acta* 69, 4485–4494.

861 Halicz L., Galy A., Belshaw N.S., O’Nions R.K., 1999. High-precision measurement of Ca-isotopes in
862 carbonates and related materials by multiple collector inductively coupled plasma mass
863 spectrometry (MC-ICP-MS). *Journal of Analytical Atomic Spectrometry* 14, 1835-1838.

864 He, D., Zhu, Z., Zhao, L., Belshaw, N.S., Zheng, H., Li, X., Hu, S., 2019. A practical method for
865 measuring high precision calcium isotope values without chemical purification for calcium
866 carbonate samples by multiple collector inductively coupled plasma mass spectrometry. *Chem.*
867 *Geol.* 514, 105-111.

868 Hensley, T.M., 2006. Calcium Isotopic Variation in Marine Evaporites and Carbonates: Applications
869 to Late Miocene Mediterranean Brine Chemistry and Late Cenozoic Calcium Cycling in the
870 Oceans. Ph.D. Dissertation, University of California, San Diego, 124pp.

871 Heuser, A., Eisenhauer, A., Gussone, N., Bock, B., Hansen, B.T., Nägler, T.F., 2002. Measurement of
872 calcium isotopes ($\delta^{44}\text{Ca}$) using a multicollector TIMS technique. *International Journal of Mass*
873 *Spectrometry* 220, 385-397.

874 Hindshaw, R.S., Reynolds, B.C., Wiederhold, J.G., Kretzschmar, R., Bourdon, B., 2011. Calcium
875 isotopes in a proglacial weathering environment: Damma glacier, Switzerland. *Geochim.*
876 *Cosmochim. Acta* 75, 106-118.

877 Hindshaw, R.S., Bourdon, B., von Strandmann, P.A.P., Vigier, N., Burton, K.W., 2013. The stable
878 calcium isotopic composition of rivers draining basaltic catchments in Iceland. *Earth Planet. Sci.*
879 *Lett.* 374, 173-184.

880 Hindshaw, R. S., Rickli, J., Leuthold, J., Wadham, J., Bourdon, B., 2014. Identifying weathering
881 sources and processes in an outlet glacier of the Greenland Ice Sheet using Ca and Sr isotope
882 values. *Geochim. Cosmochim. Acta* 145, 50-71.

883 Hogan, J.F., Blum, J.D., Siegel, D.I., Glaser, P.H., 2000. $^{87}\text{Sr}/^{86}\text{Sr}$ as a tracer of groundwater discharge
884 and precipitation recharge in the Glacial Lake Agassiz Peatlands, northern Minnesota. *Water*
885 *Resources Research* 36, 3701-3710.

886 Holmden, C., Bélanger, N., 2010. Ca isotope cycling in a forested ecosystem. *Geochim. Cosmochim.*
887 *Acta* 74, 995-1015.

888 Ibáñez, C., Prat, N., Cancio, A., 1996. Changes in the hydrology and sediment transport produced by
889 large dams on the lower Ebro river and its estuary. *Regulated Rivers* 12, 51-62.

890 INE., Censo Agrario. Instituto Nacional de Estadística. [CD-ROM], Madrid, 2003.

891 Jacobson, A.D., Holmden, C., 2008. $\delta^{44}\text{Ca}$ evolution in a carbonate aquifer and its bearing on the
892 equilibrium isotope fractionation factor for calcite. *Earth Planet. Sci. Lett.* 270, 349-353.

893 Jacobson, A.D., Andrews, M.G., Lehn, G.O., Holmden, C., 2015. Silicate versus carbonate weathering
894 in Iceland: New insights from Ca isotopes. *Earth Planet. Sci. Lett.* 416, 132-142.

895 Kreissig, K., Elliott, T., 2005. Ca isotope fingerprints of early crust-mantle evolution. *Geochim.*
896 *Cosmochim. Acta* 69, 165-176.

897 Langmuir, C.H., Vocke, R.D., Hanson, G.N., 1978. A general mixing equation with application to
898 Icelandic basalts. *Earth Planet. Sci. Lett.* 37, 380-392.

899 Lemarchand, D., Wasserburg, G.J., Papanastassiou, D.A., 2004. Rate-controlled calcium isotope
900 fractionation in synthetic calcite. *Geochim. Cosmochim. Acta* 68, 4665-4678.

901 Li, J., DePaolo, D.J., Wang, Y., Xie, X., 2018. Calcium isotope fractionation in a silicate dominated
902 Cenozoic aquifer system. *J. Hydrol.* 559, 523-533.

903 Lu, W.N., He, Y., Wang, Y., Ke, S., 2020. Behavior of calcium isotopes during continental subduction
904 recorded in meta-basaltic rocks. *Geochim. Cosmochim. Acta* 278, 392-404.

905 Millot R., Gaillardet J., Dupré B., Allègre C.J., 2003. Northern latitude chemical weathering rates:
906 clues from the Mackenzie River Basin, Canada. *Geochim. Cosmochim. Acta* 67, 1305-1329.

907 Millot, R., Négrel, Ph., Petelet-Giraud, E., 2007. Multi-isotopic (Li, B, Sr, Nd) approach for
908 geothermal reservoir characterization in the Limagne Basin (Massif Central, France). *Applied*
909 *Geochemistry* 22, 2307-2325.

910 Moore, J., Jacobson, A.D., Holmden, C., Craw, D., 2013. Tracking the relationship between mountain
911 uplift, silicate weathering, and long-term CO₂ consumption with Ca isotopes: Southern Alps, New
912 Zealand. *Chem. Geol.* 341, 110-127.

913 Négrel, Ph., Allègre, C.J., Dupré, B., Lewin, E., 1993. Erosion sources determined from inversion of
914 major, trace element values and strontium isotopic values in riverwater: the Congo Basin case.
915 *Earth Planet. Sci. Lett.* 120, 59-76.

916 Négrel, Ph., Fouillac, C., Brach, M., 1997. A strontium isotopic study of mineral and surface waters
917 from the Cézaillier (Massif Central, France): implications for mixing processes in areas of
918 disseminated emergences of mineral waters. *Chem. Geol.* 135, 89-101.

919 Négrel, Ph., Grosbois, C., Kloppmann, W., 2000. The labile fraction of suspended matter in the Loire
920 River (France): multi-element chemistry and isotopic (Rb–Sr and C–O) systematics. *Chem. Geol.*
921 166, 271-285.

922 Négrel, Ph., Roy, S., Petelet-Giraud, E., Millot, R., Brenot, A., 2007. Long term fluxes of dissolved
923 and suspended matter in the Ebro River Basin (Spain). *J. Hydrol.* 342, 249-260.

924 Négrel, Ph., Millot, R., Brenot, A., Bertin, C., 2010. Lithium isotopes as tracers of groundwater
925 circulation in a peat land. *Chem. Geol.* 276, 119-127.

926 Négrel, Ph., Petelet-Giraud, E., Millot, R., 2016. Tracing water cycle in regulated basin using stable
927 $\delta^{18}\text{O}$ – $\delta^2\text{H}$ isotopes: The Ebro river basin (Spain). *Chem. Geol.* 422, 71-81.

928 Négrel, Ph., Grosbois, C., 1999. Changes in chemical and $^{87}\text{Sr}/^{86}\text{Sr}$ signature distribution patterns of
929 suspended matter and bed sediments in the upper Loire river basin (France). *Chem. Geol.* 156, 231-
930 249.

931 Novak, M., Holmden, C., Farkaš, J., Kram, P., Hruska, J., Curik, J., Veselovsky, F., Stepanova, M.,
932 Kochergina, Y.V., Erban, V., Fottova D., Simecek, M., Bohdalkova, L., Prechova E., Voldrichova,
933 P., Cernohous, V., 2020. Calcium and strontium isotope dynamics in three polluted forest
934 ecosystems of the Czech Republic, Central Europe. *Chem. Geol.* 119472.

935 Palmer, M.R., Edmond, J.M., 1992. Controls over the strontium isotope composition of river water.
936 *Geochim. Cosmochim. Acta* 56, 2099-2111.

937 Parkhurst, D.L., Appelo, C.A.J., 1999. User's guide to PHREEQC (Version 2): A computer program
938 for speciation, batch-reaction, one-dimensional transport, and inverse geochemical calculations.
939 *Water-Resources Investigations Report*, 99, 4259, 312pp.

940 Petelet-Giraud, E., Négrel, Ph., Casanova, J., 2003. Variability of $^{87}\text{Sr}/^{86}\text{Sr}$ in water draining granite
941 revealed after a double correction for atmospheric and anthropogenic inputs. *Hydrological Sciences*
942 *Journal* 48, 729-742.

943 Petelet-Giraud, E., Négrel, Ph., 2011. Dissolved fluxes of the Ebro river basin (Spain): impact of main
944 lithologies and role of tributaries. D. Barcelo and M. Petrovic (eds.). The Ebro River Basin.
945 Springer-Verlag Berlin Heidelberg 2010. Handbook of Environmental Chemistry 13, 97–120.

946 Pin, C., Bassin, C., 1992. Evaluation of a strontium specific extraction chromatographic method for
947 isotopic analysis in geological materials. *Analytica Chimica Acta* 269, 249-255.

948 Prats, J., Val, R., Armengol, J., Dolz, J., 2010. Temporal variability in the thermal regime of the lower
949 Ebro River (Spain) and alteration due to anthropogenic factors. *J. Hydrol.* 387, 105–118.

950 Rudnick, R.L., Gao, S., 2003. Composition of the continental crust. In Holland, H.D., Turekian, K.K.
951 and Rudnick, R.L. (Eds.), *Treatise on Geochemistry, the Crust*, vol. 3, Elsevier-Pergamon, Oxford
952 (2003), pp.1-64.

953 Ryu, J.S., Jacobson, A.D., Holmden, C., Lundstrom, C., Zhang, Z., 2011. The major ion, $\delta^{44/40}\text{Ca}$,
954 $\delta^{44/42}\text{Ca}$, and $\delta^{26/24}\text{Mg}$ geochemistry of granite weathering at pH=1 and T=25 °C: power-law
955 processes and the relative reactivity of minerals. *Geochim. Cosmochim. Acta* 75, 6004-6026.

956 Scheuermann, P.P., Syverson, D.D., Higgins, J.A., Pester, N.J., Seyfried Jr, W.E., 2018. Calcium
957 isotope systematics at hydrothermal conditions: Mid-ocean ridge vent fluids and experiments in the
958 $\text{CaSO}_4\text{-NaCl-H}_2\text{O}$ system. *Geochim. Cosmochim. Acta* 226, 18-35.

959 Schmitt, A.D., Chabaux, F., Stille, P., 2003a. The calcium riverine and hydrothermal isotopic fluxes
960 and the oceanic calcium mass balance. *Earth Planet. Sci. Lett.* 213, 503-518.

961 Schmitt, A.D., Stille, P., Vennemann, T., 2003b. Variations of the $^{44}\text{Ca}/^{40}\text{Ca}$ ratio in seawater during
962 the past 24 million years: evidence from $\delta^{44}\text{Ca}$ and $\delta^{18}\text{O}$ values of Miocene phosphates. *Geochim.*
963 *Cosmochim. Acta* 67, 2607-2614.

964 Schmitt, A.D., Stille, P., 2005. The source of calcium in wet atmospheric deposits: Ca-Sr isotope
965 evidence. *Geochim. Cosmochim. Acta* 69, 3463-3468.

966 Schmitt, A.D., Vigier, N., Lemarchand, D., Millot, R., Stille, P., Chabaux, F., 2012. Processes
967 controlling the stable isotope compositions of Li, B, Mg and Ca in plants, soils and waters: A
968 review. *CR Geoscience* 344, 704-722.

969 Shouakar-Stash, O., Kharaka, Y., Koopmann, R., Harmon, R., Négrel, Ph., Wanty, R.B., 2018. A
970 remembrance of Thomas (Tom) Bullen, 1951-2018. *App. Geochem.* 98, 474–475.

971 Skulan, J., DePaolo, D.J., Owens, T.L., 1997. Biological control of calcium isotope abundances in the
972 global calcium cycle, *Geochim. Cosmochim. Acta* 61, 2505–2510.

973 Soler, A., Canals, A., Goldstein, S. L., Otero, N., Antich, N., Spangenberg, J., 2002. Sulfur and
974 strontium isotope composition of the Llobregat River (NE Spain): tracers of natural and
975 anthropogenic chemicals in stream waters. *Wat. Air Soil Poll.* 136, 207-224.

976 Soudry, D., Segal, I., Nathan, Y., Glenn, C.R., Halicz, L., Lewy, Z., VonderHaar, D.L., 2004.
977 $^{44}\text{Ca}/^{42}\text{Ca}$ and $^{143}\text{Nd}/^{144}\text{Nd}$ isotope variations in Cretaceous–Eocene Tethyan francolites and their
978 bearing on phosphogenesis in the southern Tethys. *Geol.* 32, 389-392.

- 979 Subías, I., Moritz, R., Fernández-Nieto, C., 1998. Isotopic composition of strontium in the Valle de
980 Tena (Spanish Central Pyrenees) fluorite deposits: relevance for the source of elements and genetic
981 significance. *Mineral. Dep.* 33, 416-424.
- 982 Tang, J., Dietzel, M., Böhm, F., Köhler, S.J., Eisenhauer, A., 2008. $\text{Sr}^{2+}/\text{Ca}^{2+}$ and $^{44}\text{Ca}/^{40}\text{Ca}$
983 fractionation during inorganic calcite formation: II. Ca isotopes. *Geochim. Cosmochim. Acta* 72,
984 3733-3745.
- 985 Tipper, E.T., Galy, A., Bickle, M.J., 2006. Riverine evidence for a fractionated reservoir of Ca and Mg
986 on the continents: implications for the oceanic Ca cycle. *Earth Planet. Sci. Lett.* 247, 267-279.
- 987 Tipper, E.T., Gaillardet, J., Galy, A., Louvat, P., Bickle, M.J., Capmas, F., 2010. Calcium isotope
988 values in the world's largest rivers: a constraint on the maximum imbalance of oceanic calcium
989 fluxes. *Global Biogeochem. Cycles* GB3019, 24(3).
- 990 Tipper, E.T., Schmitt, A.D., Gussone, N., 2016. Global Ca cycles: coupling of continental and oceanic
991 processes. In *Calcium Stable Isotope Geochemistry* (pp. 173-222). Springer, Berlin, Heidelberg.
- 992 Veizer, J., 1989. Strontium isotopes in seawater through time. *Annual Review of Earth and Planetary*
993 *Sci.* 17, 141-167.
- 994 Wiederhold, J.G., 2015. Metal stable isotope signatures as tracers in environmental geochemistry.
995 *Env. Sci. Tech.* 49, 2606-2624.
- 996 Wei, G., Ma, J., Liu, Y., Xie, L., Lu, W., Deng, W., Ren, Z., Zeng, T., Yang, Y., 2013. Seasonal
997 changes in the radiogenic and stable strontium isotopic composition of Xijiang River water:
998 Implications for chemical weathering. *Chem. Geol.* 343, 67-75.
- 999 Wiegand, B.A., Chadwick, O.A., Vitousek, P.M., Wooden, J.L., 2005. Ca cycling and isotopic fluxes
1000 in forested ecosystems in Hawaii. *Geoph. Res. Lett.* 32, L11404, doi:10.1029/2005GL022746.
- 1001 Wiegand, B.A., Schwendenmann, L., 2013. Determination of Sr and Ca sources in small tropical
1002 catchments (La Selva, Costa Rica)—A comparison of Sr and Ca isotopes. *J. Hydrol.* 488, 110-117.
- 1003 Zhu, P., Macdougall, J.D., 1998. Calcium isotopes in the marine environment and the oceanic calcium
1004 cycle. *Geochim. Cosmochim. Acta* 62, 1691-1698.